MOX-Report No. 66/2025

A topology optimization framework for scaffold design in soilless cultivation

Speroni, G.; Mondini, N.; Ferro, N.; Perotto, S.

A topology optimization framework for scaffold design in soilless cultivation

Giacomo Speroni[1], Nicolò Mondini[1], Nicola Ferro[2], Simona Perotto[1]

[1]MOX - Dipartimento di Matematica Politecnico di Milano
Piazza L. da Vinci, 32, I-20133 Milano, Italy
`{giacomo.speroni, nicolo.mondini, simona.perotto}@polimi.it`

[2]Dipartimento di Scienze Molecolari e Nanosistemi
Università Ca' Foscari,
Via Torino, 155, Venezia Mestre, 30170, Italy
`nicola.ferro@unive.it`

Abstract

In this work, we customize the `microSIMPATY` algorithm, combining Solid Isotropic Material with Penalization (SIMP) topology optimization with anisotropic mesh adaptation, within a multi-physics framework to design cellular material scaffolds suitable for soilless cultivation systems. The design of these novel substrates is driven by optimization criteria that balance mechanical and fluid-dynamic performance, with the aim of effectively supporting plant growth. The numerical validation results and the *in silico* root growth simulations carried out in virtual vase-like containers confirm promising potential toward replacing conventional organic and inorganic substrates with an optimized, sustainable, and readily accessible alternative.

Keywords: Material design, Multi-physics topology optimization, Inverse homogenization, Anisotropic mesh adaptation, Soilless agriculture

1 Introduction

The rapid increase in global food demand driven by projected population growth [1, 2] poses critical challenges to modern agriculture [3, 4]. Traditional agricultural methods are increasingly unable to scale in a sustainable manner due to their high land and water demands and limited resource efficiency [5]. Meeting these challenges requires cultivation strategies that maximize productivity while minimizing land and environmental impact [6]. In this context, soilless agriculture has emerged as a promising solution to decouple food production from arable land availability [7, 8]. By enabling cultivation under controlled environmental conditions, soilless agriculture systems improve resource efficiency, crop uniformity, and yield predictability [9, 10].

Hydroponics, one of the main techniques in soilless agriculture, stands out for its productivity and versatility, relying on a supporting matrix, called substrate, that provides mechanical anchorage while enabling air and nutrient circulation through water [11, 12, 13, 14]. A wide range of substrates is currently used in hydroponic systems, each characterized by distinct physical and chemical properties. For instance, peat moss and coconut coir are valued for their high water-holding capacity and aeration balance, but raise sustainability concerns due to non-renewable sourcing or intensive processing [15, 16]. Perlite and vermiculite offer low density and excellent root aeration yet generate significant waste and are difficult to recycle [17, 16]. Rock wool, widely adopted in industrial setups, ensures good moisture retention and structural stability but suffers from poor biodegradability and high disposal costs [18, 19]. More recently, hydrogels have been explored as partially renewable alternatives, though challenges remain in ensuring consistent mechanical strength and nutrient diffusion [20, 21]. The strengths and shortcomings of these conventional materials emphasize the necessity for innovative substrate designs, with desired properties including structural robustness, fluid dynamics, chemical, thermal, and electrical characteristics, aeration capacity, controlled porosity, manufacturability and recyclability.

This work aims to foster sustainable innovation in soilless cultivation by developing advanced design methodologies for novel growth substrates, in line with the United Nations Sustainable Development Goals on Zero Hunger (SDG 2), Sustainable Cities and Communities (SDG 11), and Responsible Consumption and Production (SDG 12). Specifically, the proposed framework enables the design of engineered cellular materials with tunable permeability, mechanical integrity, and biodegradability, supporting efficient plant growth while minimizing environmental impact. This versatility has been successfully exploited in several application domains, such as biomedicine [22, 23], automotion [24], and aerospace engineering [25], but, to the best of our knowledge, has not yet been explored in the context of substrates for soilless agriculture. Accordingly, our goal is to determine the optimal unit cell topology that imparts the cellular material with the desired properties for application in soilless agriculture, with particular emphasis on ensuring efficient plant support and nutrient transport.

The optimized unit cells are generated through an automated design pipeline combining topology optimization, homogenization techniques and anisotropic mesh adaptation. In more detail, topology optimization represents a well-established framework across several branches of industrial and mechanical design [26, 27], aimed at determining the optimal distribution of material and void within a prescribed design domain in order to match a desired performance measure under specific constraints. Among the various techniques proposed in the literature (including density-based [28], level-set [29], topological derivative [30], phase-field [31], and evolutionary [32] approaches), we adopt the Solid Isotropic Material with Penalization (SIMP) method [28].

Homogenization theory provides a rigorous mathematical framework to link microstructural and macroscopic behavior in cellular materials. In direct homogenization, the effective macroscopic properties are derived by averaging the response of a given microstructure [33]. Inverse homogenization operates in the opposite direction, determining the optimal unit cell architecture that yields a prescribed set of effective (homogenized) properties at the macroscale [34].

Anisotropic mesh adaptation is a well-established technique, now integrated into many research and commercial software, to enhance the accuracy of numerical simulations with affordable computational cost. In the context of engineered cellular materials, anisotropically adapted meshes have proven highly effective in sharply resolving material–void interfaces, yielding clear and well-defined designs that are essentially ready for manufacturing.

In particular, in [35] the authors introduced the `microSIMPATY` algorithm, which discretizes an inverse homogenization topology optimization problem using anisotropic meshes specifically tailored to the optimized unit cell. The method builds on a mathematically rigorous framework grounded in an a posteriori recovery-based anisotropic error estimator [36]. Limited two-dimensional settings, the `microSIMPATY` algorithm has been successfully applied to the design of cellular materials in both single- and multi-physics contexts [35, 22, 37, 23, 38]. The algorithm exhibits remarkable features, including minimal need for density filtering and post-processing, a largely automated optimization workflow governed by only a few control parameters, the ability to generate unconventional topologies that expand the attainable design space, all within a framework of computational burden reduction and solution quality enhancement.

In the present work, we extend this design pipeline to a fully three-dimensional setting and apply it to the design of substrates in soilless agriculture. The generalization from a two-dimensional to a three-dimensional setting turned out to be non-trivial, due to the need to handle adapted meshes within a periodic framework intrinsic to cellular material architecture. This issue demanded the development of the dedicated meshing techniques in [39].

The paper is structured as follows. Section 2 introduces the proposed framework for unit cell design, leading to the three-dimensional multi-physics extension of the `microSIMPATY` algorithm. In Section 3, we present the governing models and numerical assessments for single-physics cases, distinguishing between linear elasticity and Darcy–Stokes flow regime. Section 4 extends the design pipeline to a coupled multi-physics setting, where mechanical and fluid-dynamic requirements are simultaneously enforced. Sections 5 and 6 address the reference application of this study, focusing on the design of a new substrate for soilless agriculture and its *in silico* validation for the growth of a representative plant species from the *Brassicaceae* family. Finally, Section 7 summarizes the main findings and outlines future research directions.

2 Cell design

Cellular materials benefit from the interplay between distinct spatial scales, namely the macroscopic scale of a specimen Ω and the periodic micro-architecture of a representative unit cell ω. To consistently link these scales, it is customary to employ direct and inverse homogenization techniques.

The direct approach replaces the heterogeneous material constituting Ω with an equivalent homogeneous medium whose effective properties encode the impact of the repeated micro-geometry ω onto Ω [40, 41, 42, 33]. Thus, direct homogenization provides a rigorous micro-to-macro upscaling for quantities of interest (e.g., elastic stiffness, hydraulic permeability) while preserving the essential behaviour of the heterogeneous material at a contained modeling effort. Inverse homogenization reverses the perspective. For assigned target properties (e.g., a desired elastic or permeability tensor) for the material in Ω, the goal is to identify a periodic unit cell ω whose homogenized properties match the selected target quantities [34, 29]. In such a context, a possible choice for the design of ω is represented by topology optimization, which allows for the proposal of unconventional freeform designs, as an alternative to the optimization of predefined unit cells (e.g., triply periodic minimal surfaces [43] or truss-based optimization [44, 45]). In more detail, topology optimization aims to distribute material and void portions within ω in order to optimize a performance measure under design and physical constraints. Among the several topology optimization methods available in the literature, we adopt the density-based Solid Isotropic Material with Penalization (SIMP) method [46], whose generic form is

$$\min_{\rho \in R} \mathcal{J}(\mathbf{U}(\rho), \rho) \; : \begin{cases} \mathcal{A}_\rho(\mathbf{U}(\rho), \mathbf{V}) = \mathcal{F}_\rho(\mathbf{V}) \quad \forall \mathbf{V} \in V \\ \underline{\mathbf{c}} \leq \mathbf{C}(\mathbf{U}(\rho), \rho) \leq \overline{\mathbf{c}} \\ \rho \in [\underline{\rho}, 1], \end{cases} \tag{1}$$

where ρ models the distribution of the material density in the design domain ω ($\rho = \underline{\rho}$ for the void portions, $\rho = 1$ for full material and $\underline{\rho} < \rho < 1$ for intermediate densities). In particular, functional $\mathcal{J}$ denotes the selected performance measure (e.g., mass, inverse permeability, bulk compressibility), possibly depending on the density ρ and the state $\mathbf{U}$; the first constraint takes into account the physical model underlying the design process, where $\mathcal{A}_\rho(\cdot, \cdot)$ and $\mathcal{F}_\rho(\cdot)$

define the associated differential weak forms; the second constraint enforces two-sided controls on quantities depending on the state and/or the density variables through vector $\mathbf{C}$, $\underline{\mathbf{c}}$ and $\overline{\mathbf{c}}$ gathering the corresponding lower and upper bounds; the employment of a minimum material density value $\underline{\rho}$ (set to 0.001 throughout the paper) in the third constraint guarantees that problem (1) is well-defined. Finally, V is an appropriate configuration-dependent space, while R coincides with $L^\infty(\omega, [0, 1])$, standard notation being adopted for function spaces [47].

In practice, consistently with [48, 49, 33], we discretize problem (1) through continuous linear finite elements, after introducing a conforming tetrahedral computational mesh, $\mathcal{T}_h$, of ω of cardinality $\#\mathcal{T}_h$. The transition from the continuous to the discrete setting introduces well-known numerical challenges, such as mesh dependency (the optimized layout depends on the computational grid) and checkerboard patterns (associated with the presence of weakly-connected solid elements). A variety of remedies to mitigate these issues is available in the literature, including density filters (e.g., Helmholtz- or Heaviside-type [50]), robust formulations [51, 52], high-order approximations [53, 54], as well as adapted meshes [55, 56].

With reference to the design of cellular materials, functional $\mathcal{J}$ and the constraint vector $\mathbf{C}$ in (1) are related to the target quantities assigned to Ω, the differential forms $\mathcal{A}_\rho$ and $\mathcal{F}_\rho$ are associated with the homogenization process, whereas function spaces R and V properly include periodic boundary conditions. This set of choices classifies problem (1) as an inverse homogenization topology optimization approach (see the next sections for the details). The discrete counterpart of this problem is tackled through the `microSIMPATY` algorithm proposed in [35], which enriches inverse homogenization topology optimization with a combination of anisotropic mesh adaptation and density filtering. `microSIMPATY` algorithm guarantees a sharp detection of the structural boundary through highly-stretched tetrahedra (with few degrees of freedom crowded at the material/void interface), while generating innovative cellular layouts [22, 37, 23, 38].

In Algorithm 1 we extend `microSIMPATY` to a three-dimensional (3D) setting, with a view to an effective application to the design of innovative substrates for soilless agriculture. Concerning the input values, we distinguish among: parameters $\mathcal{J}$, $\mathbf{C}$, $\mathcal{G}$, $\underline{\mathbf{c}}$, $\overline{\mathbf{c}}$ specifying problem (1), where $\mathcal{G}$ collects the derivatives of the functionals $\mathcal{J}$ and $\mathbf{C}$ with respect to ρ; the initial guess for the discretization of ω ($\mathcal{T}_h^0$) and of the density function (ρ_h^0); vector $\mathbf{H} = [r, \beta, \eta]^T$ collecting the main quantities involved in the density filters; tolerances `TOTOL`, `TAU`, `ATOL`, and integers `TOIT`, `AIT` constraining the optimization and adaptation procedures; lengths $h_{\min}$ and $h_{\max}$ defining the minimum and maximum allowed mesh element size.

The main loop of the algorithm (lines 3–12) includes an optimization, a filtering, and a mesh adaptation phases, constrained by a maximum number `AIT` of allowed iterations and a control on the stagnation of the mesh cardinality within tolerance `ATOL` (line 3).

In more detail, routine `optimize` (line 4) implements the optimization process through the consolidated Method of Moving Asymptotes (MMA) [57, 58], taking into account the performance measure $\mathcal{J}$ and the constraint vector $\mathbf{C}$, together with the associated derivatives in $\mathcal{G}$. This phase returns the number `nOpt` of performed optimization loops together with the updated density function, subject to a prescribed tolerance `TOTOL` for accuracy and a maximum number of iterations `TOIT`.

The filtering phase is performed by routine `filter` (line 5), which resorts to two standard filters [59], whose combined action enhances a sharp material/void alternation. First, a Helmholtz smoothing operator removes excessively thin features by promoting intermediate densities along the layout contour. To this aim, the input density ρ is updated into the smoothed quantity $\hat{\rho}$ solution to the partial differential equation (PDE)

$$-r\Delta\hat{\rho} + \hat{\rho} = \rho \quad \text{in } \omega, \tag{2}$$

to be completed with suitable boundary conditions, where $r \in \mathbf{H}$ is a length parameter related to the radius of a circular mollifier. Subsequently, $\hat{\rho}$ is sharpened through the Heaviside filter as

$$\tilde{\rho} = \frac{\tanh(\beta\eta) + \tanh[\beta(\hat{\rho} - \eta)]}{\tanh(\beta\eta) + \tanh[\beta(1 - \eta)]}, \tag{3}$$

with β, $\eta \in \mathbf{H}$ tuning the severity of the sharpening to enhance the contrast between void and full material towards a black-and-white configuration.

Algorithm 1 `microSIMPATY`

```
Input: $\mathcal{J}$, $\mathbf{C}$, $\mathcal{G}$, $\underline{\mathbf{c}}$, $\overline{\mathbf{c}}$, $\mathcal{T}_h^0$, $\rho_h^0$, $\mathbf{H}$, TOTOL, TAU, ATOL, TOIT, AIT, $h_{\min}$, $h_{\max}$
Set: k = 0, errA = 1+ ATOL, iter = 0;
while errA > ATOL and k < AIT do
    [nOpt, $\rho_h^{k+1}$] = optimize($\rho_h^{k}, \mathcal{J}, \mathbf{C}, \mathcal{G}, \underline{\mathbf{c}}, \overline{\mathbf{c}}$, TOTOL, TOIT);
    $\tilde{\rho}_h^{k+1}$ = filter($\rho_h^{k+1}, \mathbf{H}$);
    $\mathcal{T}_h^{k+1}$ = adapt($\mathcal{T}_h^{k}, \tilde{\rho}_h^{k+1}$, TAU, $h_{\min}, h_{\max}$);
    $\rho_h^{k+1}$ = project($\rho_h^{k+1}, \mathcal{T}_h^{k+1}$);
    $\tilde{\rho}_h^{k+1}$ = project($\tilde{\rho}_h^{k+1}, \mathcal{T}_h^{k+1}$);
    errA = $\left|\#\mathcal{T}_h^{k+1} - \#\mathcal{T}_h^{k}\right| / \#\mathcal{T}_h^{k}$;
    k = k+1;
    iter = iter + nOpt;
end while
$\mathcal{T}_h = \mathcal{T}_h^{k}$;
$\rho_h = \rho_h^{k}$;
$\tilde{\rho}_h = \tilde{\rho}_h^{k}$;
Output: $\mathcal{T}_h, \rho_h, \tilde{\rho}_h$, iter
```

The last step in the main loop coincides with a mesh adaptation process in an anisotropic setting. The corresponding output is a computational mesh whose elements are sized, shaped and oriented in order to sharply detect the material/void interface at a contained computational effort (see the literature related to the design of structures and materials [60, 35]). In particular, routine `adapt` implements a metric-based approach for mesh generation [61, 62] where the mesh metric is based on the anisotropic counterpart of the well-established Zienkiewicz-Zhu error estimator [63, 64], proposed in [36, 65]. The choice of this specific error estimator is motivated by its ability to sharply capture steep solution gradients, thereby meeting the need to accurately track the sharp boundaries of the structure under optimization. The transition from the estimator to the metric is carried out by solving local constrained minimization problems, aiming to guarantee a prescribed accuracy `TAU` on the density gradient, while minimizing the mesh cardinality and equidistributing the error estimator across the computational grid. To avoid the generation of excessively small or large tetrahedra, we lower and upper bound the element size through the prescribed lengths $h_{\min}$ and $h_{\max}$.

The **while** loop of the algorithm is completed by a projection step through routine `project` (lines 7-8), which ensures the consistency of the discrete material density with the current computational mesh. Algorithm 1 returns the final anisotropic adapted mesh, the material and the filtered densities, together with the cumulative number of performed optimization iterations.

We observe that `microSIMPATY` algorithm features a mild coupling between the optimization and adaptation modules, aimed at mitigating the overall computational burden. Indeed, parameters `TOTOL` and `TOIT` can be effectively used to regulate the alternation between optimization and adaptation steps. Moreover, the imposition of periodic boundary conditions in spaces R and V introduces an additional layer of complexity when dealing with adapted meshes. In practice, periodicity must be enforced simultaneously across opposite faces, edges, and corners of the domain, which substantially increases the technical difficulty and limits the availability of suitable 3D meshing tools. To address this challenge, we employ a dedicated routine for periodic mesh adaptation, recently introduced in [39].

Concerning the implementation of Algorithm 1, we primarily rely on `Python 3.11.7` and `FreeFEM` [66]. We exploit `dolfinx` [67] for partial differential equation–constrained optimization, where computations are executed in parallel with `PETSc` in its `Python` interface [68], providing the linear algebra backend and scalable solvers. Boundary conditions are enforced through the `dolfinx_mpc`[1] library, which enables an efficient parallel treatment of periodicity via multi-point constraints. As for the mesh adaptation step, the anisotropic metric tensor is computed in parallel using `FreeFEM`, while the generation of periodic adapted meshes is assigned to `mmg` [69], an open-source tool specialized in anisotropic grid handling.

This modular integration provides an automatic, efficient, robust and flexible tool for the design of innovative engineered cellular materials.

3 Single-physics-constrained setting

This section tailors the design framework in (1) to two distinct settings, linear elasticity and Darcy-Stokes flow, thus highlighting the versatility of the `microSIMPATY` algorithm in addressing different engineering contexts.

3.1 The linear elasticity case

The linear elasticity theory constitutes the first physics setting adopted for the design of optimized cellular materials. In this context, the static equilibrium of the specimen Ω is modeled by the equation

$$-\nabla \cdot \sigma(\mathbf{u}) = \mathbf{f} \quad \text{in } \Omega,$$

where $\mathbf{f}$ is a volumetric forcing term and σ is the material stress, being related to the strain ε and the stiffness E, through the standard linear constitutive law

$$\sigma(\mathbf{u}) = E\varepsilon(\mathbf{u}), \qquad \varepsilon(\mathbf{u}) = \frac{1}{2}[\nabla \mathbf{u} + (\nabla \mathbf{u})^T], \tag{4}$$

with $\mathbf{u} : \Omega \to \mathbb{R}^3$ the structure displacement. In the sequel, we adopt the Voigt notation for the quantities σ, ε and E, being

$$\sigma(\mathbf{u}) = [\sigma_{11}, \sigma_{22}, \sigma_{33}, \sigma_{23}, \sigma_{13}, \sigma_{12}]^T,$$

$$\varepsilon(\mathbf{u}) = [\varepsilon_{11}, \varepsilon_{22}, \varepsilon_{33}, 2\varepsilon_{23}, 2\varepsilon_{13}, 2\varepsilon_{12}]^T,$$

$$E = [E_{ijkl}]_{ij,kl \in \mathcal{I}}\,,$$

---

[1] https://github.com/jorgensd/dolfinx_mpc

with σ_{ij}, ε_{kl}, $E_{ijkl} : \Omega \to \mathbb{R}$, for $ij, kl \in \mathcal{I} = \{11, 22, 33, 23, 13, 12\}$ [70].

Standard homogenization theory relieves us from a pointwise evaluation of relations (4). The idea is to incorporate the mechanical influence of the microscopic geometry ω into the macroscopic response of Ω by replacing the stiffness tensor E in (4) with the homogenized counterpart E^H, given by

$$E^H_{ijkl} = \frac{1}{|\omega|} \int_\omega \left[\sigma(\mathbf{u}^{0,\,ij}) - \sigma(\mathbf{u}^{*,\,ij})\right] : \left[\varepsilon(\mathbf{u}^{0,\,kl}) - \varepsilon(\mathbf{u}^{*,\,kl})\right] \,\mathrm{d}\omega, \tag{5}$$

for $ij, kl \in \mathcal{I}$, where the prescribed test fields $\mathbf{u}^{0,\,11} = [x, 0, 0]^T$, $\mathbf{u}^{0,\,22} = [0, y, 0]^T$, $\mathbf{u}^{0,\,33} = [0, 0, z]^T$, $\mathbf{u}^{0,\,23} = [0, z, 0]^T$, $\mathbf{u}^{0,\,13} = [z, 0, 0]^T$, $\mathbf{u}^{0,\,12} = [y, 0, 0]^T$ induce the microscopic corrector fields $\mathbf{u}^{*,\,ij}$ satisfying the problem

$$\int_\omega \sigma(\mathbf{u}^{*,\,ij}) : \varepsilon(\mathbf{v}) \,\mathrm{d}\omega = \int_\omega \sigma(\mathbf{u}^{0,\,ij}) : \varepsilon(\mathbf{v}) \,\mathrm{d}\omega \quad \forall \mathbf{v} \in V_\# \tag{6}$$

on the unit cell ω, with $V_\# = [H^1_\#(\omega)]^3$ the space of vector-valued periodic $H^1(\omega)$-functions. With reference to problem (1), equations (6) are strictly linked to forms $\mathcal{A}_\rho$ and $\mathcal{F}_\rho$, being

$$\mathcal{A}_\rho(\mathbf{U}(\rho), \mathbf{V}) = \int_\omega \sigma_{\tilde{\rho}}(\mathbf{u}^{*,\,ij}(\rho)) : \varepsilon(\mathbf{v}) \,\mathrm{d}\omega, \quad \mathcal{F}_\rho(\mathbf{V}) = \int_\omega \sigma_{\tilde{\rho}}(\mathbf{u}^{0,\,ij}) : \varepsilon(\mathbf{v}) \,\mathrm{d}\omega, \tag{7}$$

with $\mathbf{U}(\rho) = \mathbf{u}^{*,\,ij}(\rho)$, $\mathbf{V} = \mathbf{v}$,

$$\sigma_{\tilde{\rho}}(\cdot) = \tilde{\rho}^{\,p}\, E\boldsymbol{\varepsilon}(\cdot), \tag{8}$$

where $p \geq 1$ is the SIMP penalization exponent that mitigates intermediate densities [71], while $\tilde{\rho} = \tilde{\rho}(\rho)$ denotes the filtered density defined as in (3).

In the next two sections, different choices for $\mathcal{J}$ and $\mathbf{C}$, $\underline{\mathbf{c}}$, $\overline{\mathbf{c}}$ will lead to the design of distinct cellular materials through `microSIMPATY` algorithm. In particular, we pick the design domain $\omega \subset \mathbb{R}^3$ as the unit cube $(0, 1)^3$ and we set $p = 4$ for the SIMP penalization exponent in (8). The material selected for the unit cell is characterized by the Lamé's coefficients, λ and μ, which for an isotropic solid define the Cauchy's stress tensor in (4) as $\sigma(\mathbf{u}) = 2\mu\,\varepsilon(\mathbf{u}) + \lambda\,\mathrm{tr}(\varepsilon(\mathbf{u}))$, where $\mathrm{tr}(\cdot)$ denotes the trace operator. In the present study, we set $\lambda = 0.577$ and $\mu = 0.385$, corresponding to a unit Young's modulus and a Poisson's ratio equal to 0.3.

Concerning the input parameters of Algorithm 1, we choose a spherical material region centered in ω, whose radius varies in the specific design case, as initial guess ρ^0_h, discretized on an isotropic structured mesh $\mathcal{T}^0_h$ consisting of 162000 tetrahedra. The topology optimization step is regulated by the tolerance `TOTOL` $= 1\%$ and the maximum number of allowed iterations `TOIT` initially set to 200 and halved at each iteration `k` until 25. This choice is coherent with the pursued mild coupling paradigm involving optimization and adaptation, and allows us to reach a balance between efficiency and accuracy. The density filtering phase is tuned by the parameters in $\mathbf{H}$, here set to $r = 0.03$, $\eta = 0.5$, while β is gradually increased from 1 to 8 throughout the iterations. For mesh adaptation, we set `ATOL`$= 2\%$, `AIT`$= 10$, while prescribing `TAU`$= 10$, $h_{\max} = 0.1$ and $h_{\min} = 0.005$.

3.1.1 Design case 1

We consider a benchmark in material design, namely the maximization of the material bulk modulus. This problem is recurrent in the literature, for instance, when dealing with hierarchical laminates that can attain the Hashin–Shtrikman bounds on the bulk and shear moduli of isotropic two-phase composites [72]. This benchmark is of practical relevance for the design of load-bearing cellular materials. Indeed, maximizing the bulk modulus yields architectures suited for lightweight structural cores and energy-absorbing components [73, 74]. In the context of soilless agriculture, similar stiffness-oriented formulations can be exploited to engineer

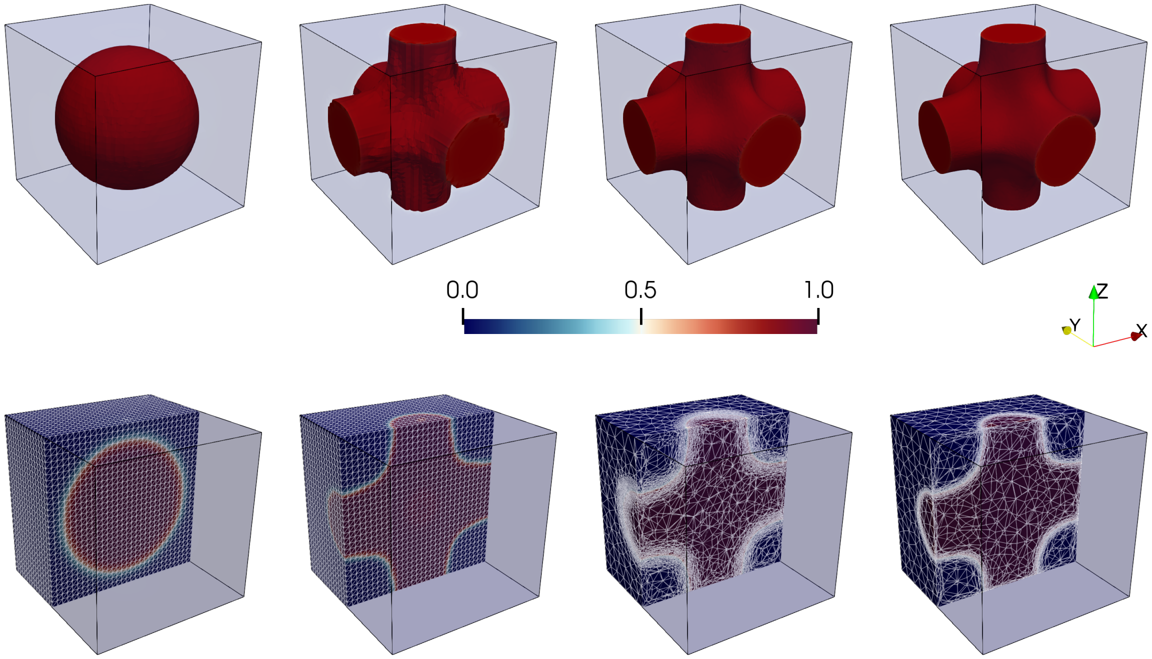

Figure 1: Design case $1_{0.3}$: density field (top) with the associated anisotropic adapted mesh overlapped (bottom) for {`iter`, `k`} = {0, 0}, {200, 0}, {300, 1}, {425, 6} (from left to right).

scaffolds that provide mechanical stability and resistance to compaction while maintaining the internal porosity required for aeration and nutrient transport.
With reference to problem (1), we choose

$$\mathcal{J}(\mathbf{u}^{*,ij}(\rho),\rho) = -\mathcal{B}(\rho), \quad \underline{c} = 0, \quad \mathrm{C}(\mathbf{u}^{*,ij}(\rho),\rho) = \mathcal{M}(\rho), \quad \overline{c} = v_f, \tag{9}$$

while defining $\mathcal{A}_\rho$ and $\mathcal{F}_\rho$ as in (7), where

$$\mathcal{B}(\rho) = \frac{1}{9}\left(E^H_{\tilde{\rho},1111} + E^H_{\tilde{\rho},2222} + E^H_{\tilde{\rho},3333}\right) + \frac{2}{9}\left(E^H_{\tilde{\rho},2233} + E^H_{\tilde{\rho},1133} + E^H_{\tilde{\rho},1122}\right)$$

denotes the (homogenized) bulk modulus, with $E^H_{\tilde{\rho},ijkl}$ the homogenized stiffness tensor components in (5) after replacing σ with $\sigma_{\tilde{\rho}}$ in (8),

$$\mathcal{M}(\rho) = \frac{1}{|\omega|}\int_\omega \tilde{\rho}\, d\omega \tag{10}$$

is the volume occupied by the material in ω, and v_f is the prescribed maximum allowed volume fraction. Notice that we constrain the design with a single two-sided inequality, so that vectors $\underline{\mathbf{c}}$, $\mathbf{C}$ and $\overline{\mathbf{c}}$ simplify to scalar quantities.

As a first scenario, denoted by Design case 1_{v_f}, we set $v_f = 0.3$, and we adopt an initial guess ρ_h^0 with a volume equal to v_f. The material topology in ω evolves towards an almost isotropic truss that distributes material along orthogonal directions (see the layouts in the first row of Fig. 1), consistently with the balanced weights across the Cartesian axes characterizing the bulk modulus definition. The benefits led by the employment of an anisotropic adapted

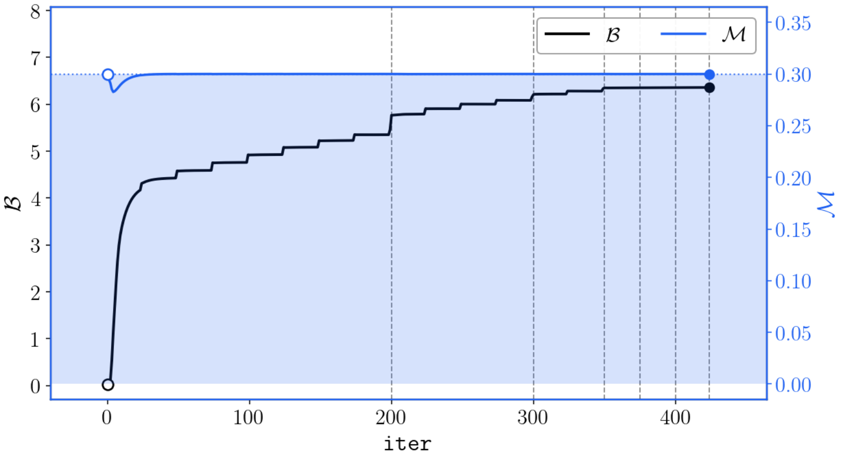

Figure 2: Design case $1_{0.3}$: evolution of the objective functional $\mathcal{B}$ and of the constraint $\mathcal{M}$ as a function of `iter`. Mesh adaptation is applied in correspondence with the vertical dashed lines.

mesh are evident in the sharply resolved structural boundary. Here the grid carefully tracks the steep material/void interface (see the second row in Fig. 1), thus limiting the presence of intermediate density values.
In Fig. 2, we show the convergence trend of functional $\mathcal{B}$ and of constraint $\mathcal{M}$. It can be observed that the bulk modulus increases, in agreement with the maximization requirement, until a stable material configuration is attained, as highlighted by the curve stagnation. The trend is not strictly monotonic and features mild jumps that can be justified by the continuation method employed to update the filter parameter β and the occurrence of mesh adaptation. We also remark that the volume constraint remains tightly enforced throughout all iterations, with $\mathcal{M}$ exactly matching the upper bound v_f at the end of the optimization process. We refer to Table 1 for further quantitative information related to $\mathcal{B}$ and $\mathcal{M}$, and to the final anisotropic adapted mesh, in terms of mesh cardinality and maximum element deformation, $s_{\max}$.

We investigate the sensitivity of the design process to the assigned volume fraction, by varying v_f in $\{0.3, 0.4, 0.5, 0.6\}$. The associated layouts are gathered in Fig. 3, first row. As v_f increases, the struts forming the unit cell remain aligned with the Cartesian directions, whereas the structural members become progressively thicker and enhance the load-bearing frames along the orthogonal directions, ultimately leading to closed-cell configurations. The transition from open to closed cells is clearly visible in the $2\times2\times2$ cell repetition displayed in the second row of the figure. The variations in the material properties for the different v_f values are confirmed in the quantities in Table 1. In particular, the effective bulk modulus increases, up to a 5×-factor, when v_f is raised, consistently with the more massive layouts of the optimized designs, while the volume constraint remains consistently satisfied. Regarding the anisotropically adapted mesh, slight variations in mesh cardinality and maximum element distortion are observed, with average values of approximately 227000 tetrahedra and 342, respectively. These results confirm that a properly adapted mesh enables the handling of heterogeneous design scenarios with comparable and still computationally affordable effort.

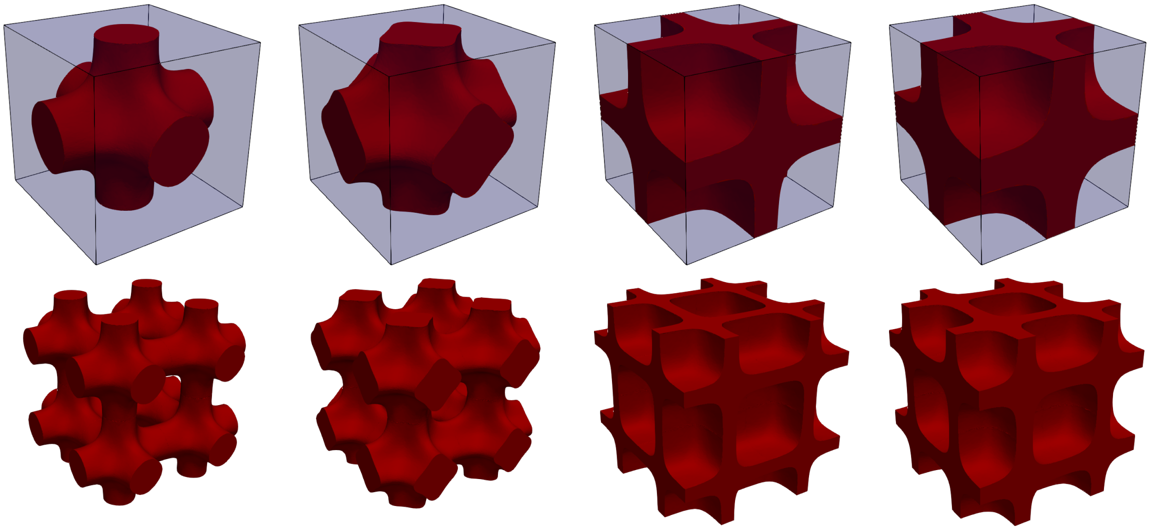

Figure 3: Design cases 1_{v_f}: unit cell (top) and associated $2 \times 2 \times 2$-layout cellular material (bottom), for $v_f \in \{0.3, 0.4, 0.5, 0.6\}$ (from left to right).

	$\mathcal{M}$	$\mathcal{B}$	$\#\mathcal{T}_h$	$s_{\max}$
Design case $1_{0.3}$				
$\underline{c}$	0	6.360	263098	371.512
C	0.300			
$\overline{c}$	0.300			
Design case $1_{0.4}$				
$\underline{c}$	0	9.400	223955	331.735
C	0.400			
$\overline{c}$	0.400			
Design case $1_{0.5}$				
$\underline{c}$	0	18.884	224983	406.274
C	0.500			
$\overline{c}$	0.500			
Design case $1_{0.6}$				
$\underline{c}$	0	26.302	200499	420.269
C	0.600			
$\overline{c}$	0.600			

Table 1: Design cases 1_{v_f}: sensitivity analysis with respect to the volume fraction.

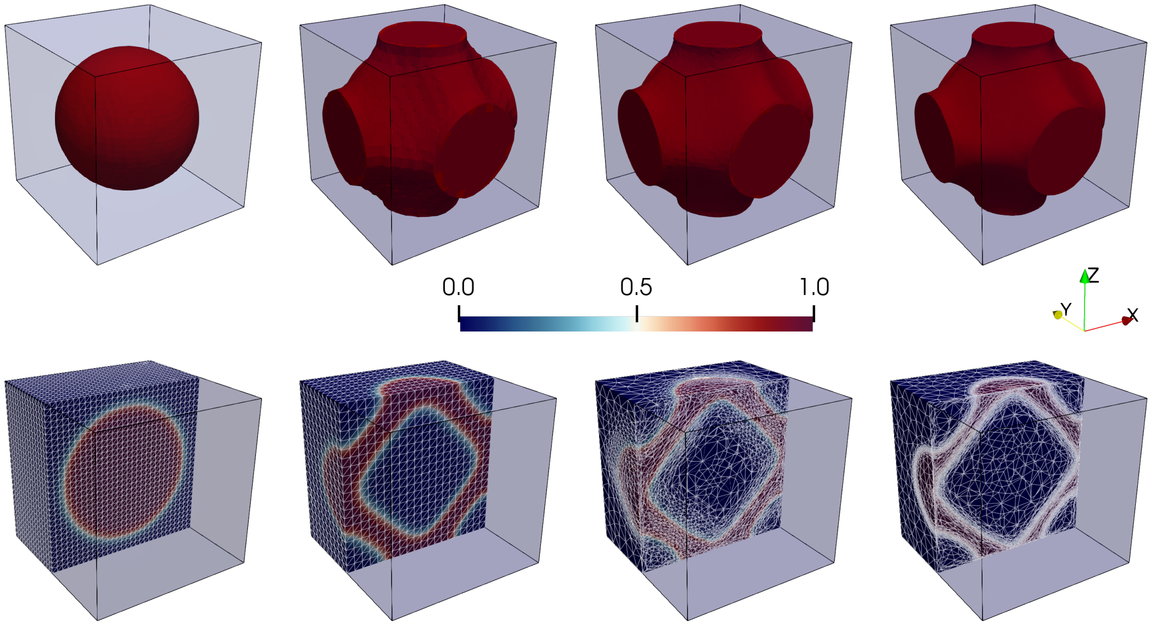

Figure 4: Design case $2_{0.0385}$: density field (top) with the associated anisotropic adapted mesh overlapped (bottom) for {`iter`, `k` } = {0, 0}, {200, 0}, {300, 1}, {446, 9} (from left to right).

3.1.2 Design case 2

As a second test case, we address a volume minimization problem under prescribed shear-stiffness constraints. This configuration promotes the formation of spanning frames and torsion-resisting members across multiple planes, while avoiding excessive rigidity in unconstrained directions. Beyond its classical relevance to lightweight structural cores and lattice reinforcements [75, 76], such a design turns out to be particularly suitable for soilless agriculture, where shear-resistant yet lightweight scaffolds can provide robust mechanical support to the plant system without compromising material efficiency. With reference to problem (1), this leads us to set

$$\mathcal{J}(\mathbf{u}^{*,ij}(\rho),\rho) = \mathcal{M}(\rho), \quad \underline{\mathbf{c}} = [\underline{E}^G_{ijij}], \quad \mathbf{C}(\mathbf{u}^{*,ij}(\rho),\rho) = [E^H_{\tilde{\rho},ijij}], \quad \overline{\mathbf{c}} = [\overline{E}^G_{ijij}],$$

where $\mathcal{M}(\rho)$ is the volume defined as in (10), while $\underline{E}^G_{ijij} = (1-\delta)\, E^G_{ijij}$ and $\overline{E}^G_{ijij} = (1+\delta)\, E^G_{ijij}$, for $ij \in \{12, 13, 23\}$, denote the three lower and upper bounds for the homogenized stiffness tensor entries related to diagonal shear, $E^H_{\tilde{\rho},ijij}$ defined as in Design case 1, with E^G_{ijij} a target value to be matched up to the tolerance $\delta = 5\%$.

The first row of Fig. 4 illustrates the evolution of the topology during optimization across the iterations for the Design case $2_{0.0385}$, corresponding to the choice $E^G_{ijij} = 0.0385$ for $ij \in \{12, 13, 23\}$. Specifically, the spherical material initial guess evolves into a truss network composed of diagonal bars, which are orthogonally connected, thus providing shear resistance on multiple planes. The iteration snapshots also highlight the beneficial effect of anisotropic mesh adaptation, as the elements progressively concentrate along the material/void interface and smooth out surface irregularities (compare the second with the third structure in the bottom row of the figure).

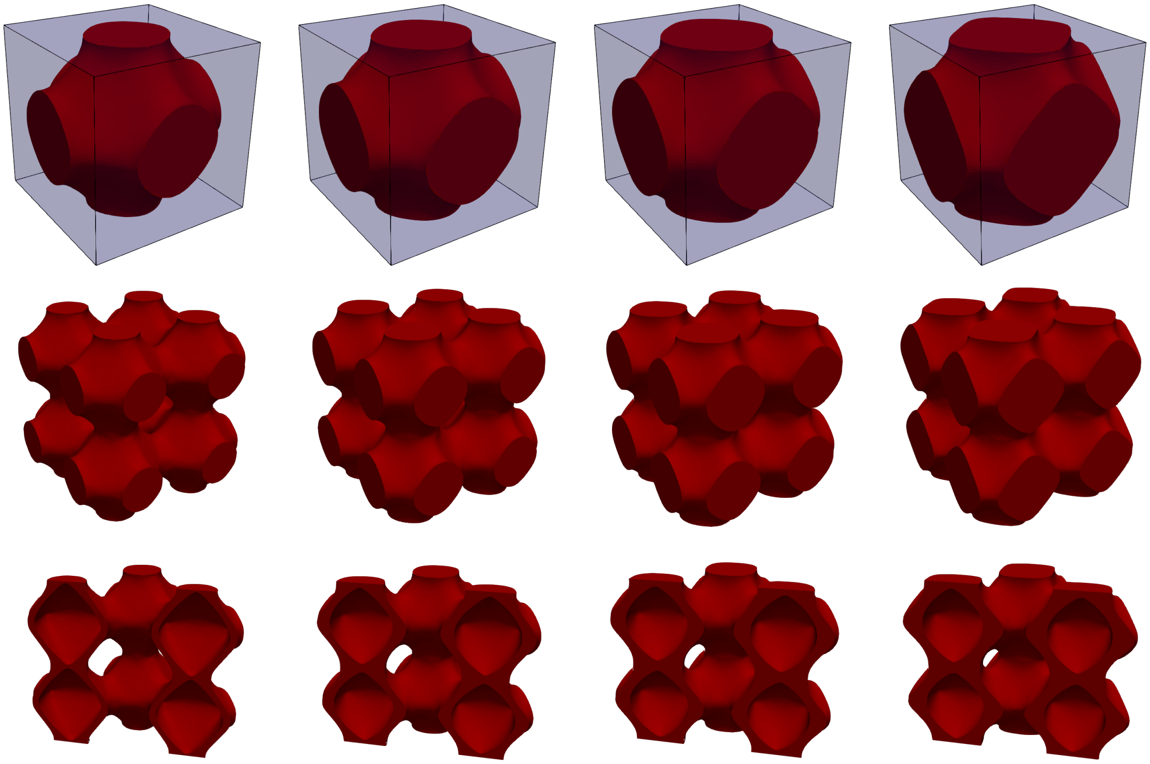

Figure 5: Design cases $2_{E^G_{ijij}}$: unit cell (top), associated $2 \times 2 \times 2$-layout (center) and clipped view (bottom) of the cellular material, for $E^G_{ijij} \in \{0.0385, 0.0577, 0.0769, 0.0962\}$ (from left to right).

We now increase the values assigned to the target shear stiffness tensor components by selecting $E^G_{ijij} \in \{0.0385, 0.0577, 0.0769, 0.0962\}$. The resulting layouts are shown in the first row of Fig. 5. It is observed that the topology is preserved, while a higher material accumulation within the domain ω results in an increase in the truss diameter. The topology invariance is also confirmed by the $2 \times 2 \times 2$ layout (second row) and by the corresponding clipped views (third row), where the presence of honeycomb-like internal void chambers is evident. Table 2 gathers the same quantities as in Table 1 for this design setting. In particular, it is observed that $\mathcal{M}$ grows with E^G_{ijij}, and that the constrained stiffness components consistently attain the prescribed lower limits, as expected from the volume minimization objective. It can also be noted that the total number of elements slightly decreases as the mass increases. This behavior is consistent with the progressive reduction of the internal void chambers, which leads to a smaller internal surface area to be resolved.

	$E^H_{\tilde{\rho},1212}$	$E^H_{\tilde{\rho},1313}$	$E^H_{\tilde{\rho},2323}$	$\mathcal{M}$	$\#\mathcal{T}_h$	$s_{\max}$
Design case $2_{0.0385}$						
$\underline{\mathbf{c}}$	0.0365	0.0365	0.0365	0.308	398692	376.440
$\mathbf{C}$	0.0365	0.0364	0.0365			
$\overline{\mathbf{c}}$	0.0404	0.0404	0.0404			
Design case $2_{0.0577}$						
$\underline{\mathbf{c}}$	0.0548	0.0548	0.0548	0.3478	316687	203.155
$\mathbf{C}$	0.0548	0.0548	0.0548			
$\overline{\mathbf{c}}$	0.0606	0.0606	0.0606			
Design case $2_{0.0769}$						
$\underline{\mathbf{c}}$	0.0731	0.0731	0.0731	0.4157	302274	126.572
$\mathbf{C}$	0.0731	0.0731	0.0731			
$\overline{\mathbf{c}}$	0.0808	0.0808	0.0808			
Design case $2_{0.0962}$						
$\underline{\mathbf{c}}$	0.0913	0.0913	0.0913	0.4716	294305	283.083
$\mathbf{C}$	0.0913	0.0913	0.0913			
$\overline{\mathbf{c}}$	0.1010	0.1010	0.1010			

Table 2: Design cases $2_{E^G_{ijij}}$: sensitivity analysis with respect to the target stiffness tensor components.

3.2 The Darcy-Stokes flow case

Analogously to Section 3.1, we here particularize problem (1) to a specific physics, now coinciding with the Darcy-Stokes setting. In this context, we deal with a fluid in a porous medium described by the flow velocity $\mathbf{w} : \Omega \to \mathbb{R}^3$ and the pressure $\pi : \Omega \to \mathbb{R}$ fields, related through the Darcy's law

$$\mathbf{w} = -K(\nabla\pi - \mathbf{g}), \qquad \nabla \cdot \mathbf{w} = 0 \quad \text{in } \Omega, \tag{11}$$

where $\mathbf{g}$ is the volumetric body force and $K : \Omega \to \mathbb{R}^{3\times 3}$ is the symmetric and positive definite permeability tensor, characterizing the resistance of the porous medium, with components $K_{ij} : \Omega \to \mathbb{R}$, for $i, j = 1, 2, 3$. Homogenization theory allows to replace tensor K with the corresponding homogenized version K^H, such that

$$K^H_{ij} = \frac{1}{|\omega|} \int_\omega \mathbf{w}^{*,i} \cdot \mathbf{e}_j \, \mathrm{d}\omega, \tag{12}$$

where $\mathbf{w}^{*,i} \in V_\#$ denotes the velocity components of the periodic pair $[\mathbf{w}^{*,i}, \pi^{*,i}]^T \in V_\# \times L^2_\#(\omega)$ solution to equations

$$\begin{cases} \displaystyle\int_\omega \nabla\mathbf{w}^{*,i} : \nabla\mathbf{v} \mathrm{d}\omega - \int_\omega \pi^{*,i} \nabla \cdot \mathbf{v} \mathrm{d}\omega + \int_\omega K^{-1}\mathbf{w}^{*,i} \cdot \mathbf{v} \mathrm{d}\omega = \int_\omega \mathbf{e}_i \cdot \mathbf{v} \mathrm{d}\omega \quad \forall \mathbf{v} \in V_\# \\ \displaystyle\int_\omega p \nabla \cdot \mathbf{w}^{*,i} \mathrm{d}\omega = 0 \quad \forall p \in L^2_\#(\omega), \end{cases} \tag{13}$$

with $\mathbf{e}_i$ the canonical unit vector, for $i = 1, 2, 3$, $V_\#$ as in Design case 1 and $L^2_\#(\omega)$ the space of the periodic square-integrable functions.

To properly define the differential problem in (1) we have to model the interplay between the filtered density $\tilde{\rho}$ in ω and the characteristics of the porous material. The idea is that equation (13) reduces to a pure Stokes flow in the regions occupied by the fluid (namely, in absence of material, being $\tilde{\rho} = 0$), while the flow velocity vanishes in correspondence with solid material areas (namely, for $\tilde{\rho} = 1$). This leads us to introduce the interpolation law

$$K_{\tilde{\rho}}^{-1} = K_{\max}^{-1} + \left(K_{\min}^{-1} - K_{\max}^{-1}\right)(1 - \tilde{\rho})\frac{1 + q}{1 - \tilde{\rho} + q}, \tag{14}$$

proposed by T. Borrvall and J. Petersson in [77]. This relation ensures a sharp distinction between fluid and solid regions through the scalar penalization parameter q (here set to 0.03) and the maximum and minimum values, $K_{\max}^{-1} = 10^6$ and $K_{\min}^{-1} = 0$, for the inverse permeability attained for $\tilde{\rho} = 1$ and $\tilde{\rho} = 0$, respectively. Now, the weak form in (1) has to be generalized to

$$\mathbf{A}_\rho(\mathbf{U}(\rho), \mathbf{V}) = [\mathcal{A}_{\rho,1}(\mathbf{U}(\rho), \mathbf{V}), \mathcal{A}_{\rho,2}(\mathbf{U}(\rho), \mathbf{V})]^T = [\mathcal{F}_{\rho,1}(\mathbf{V}), 0]^T = \mathbf{F}_\rho(\mathbf{V}), \tag{15}$$

in order to take into account the standard saddle-point formulation in (13), after replacing K^{-1} with the penalized density-dependent counterpart $K_{\tilde{\rho}}^{-1}$ in (14), being

$$\begin{aligned} \mathcal{A}_{\rho,1}(\mathbf{U}(\rho), \mathbf{V}) &= \int_\omega \nabla \mathbf{w}^{*,i}(\rho) : \nabla \mathbf{v} \mathrm{d}\omega - \int_\omega \pi^{*,i}(\rho) \nabla \cdot \mathbf{v} \mathrm{d}\omega + \int_\omega K_{\tilde{\rho}}^{-1} \mathbf{w}^{*,i}(\rho) \cdot \mathbf{v} \mathrm{d}\omega \\ \mathcal{A}_{\rho,2}(\mathbf{U}(\rho), \mathbf{V}) &= \int_\omega p \nabla \cdot \mathbf{w}^{*,i}(\rho) \mathrm{d}\omega, \quad \mathcal{F}_{\rho,1}(\mathbf{V}) = \int_\omega \mathbf{e}_i \cdot \mathbf{v} \mathrm{d}\omega, \end{aligned} \tag{16}$$

with $\mathbf{U}(\rho) = [\mathbf{w}^{*,i}(\rho), \pi^{*,i}(\rho)]^T$, $\mathbf{V} = [\mathbf{v}, p]^T \in V_\# \times L^2_\#(\omega)$.

The approximation of a saddle-point problem requires an ad-hoc choice for the discrete spaces used to approximate the velocity and the pressure in order to ensure well-posedness [78]. For this reason, in order to reduce the computational burden and to avoid spurious oscillations of the pressure, we resort to piecewise linear finite elements to discretize both the flow fields, combined with a stabilization term for the velocity [79]. When enforcing periodic boundary conditions along $\partial\omega$, the pressure is determined only up to an additive constant. To remove this indeterminacy and guarantee a unique discrete solution, we prescribe $\pi^{*,i} = 0$ at a single corner of the unit cell ω.

The Darcy–Stokes framework for inverse homogenization topology optimization here introduced provides a reference setting for the design of engineered materials with tailored fluidic properties (see, for instance, [80, 81]). In this context, we test the `microSIMPATY` algorithm under different objective functions and constraint configurations, employing the same input parameters as in Section 3.1, unless otherwise specified.

3.2.1 Design case 3

We consider a permeability–driven fluid design where the cell volume is lower-bounded. The aim is to maximize permeability in an almost isotropic manner while ensuring that the design does not degenerate into trivial, void-dominated configurations, which would arise if only an upper volume constraint were imposed. Such permeability-oriented formulations are of practical interest in the design of open-cell metallic lattices and porous scaffolds used in heat exchangers, filters, and flow-distribution systems, where uniform fluid transport and low pressure drop are essential [82, 83, 74]. Similar design principles are also increasingly relevant to soilless agriculture, where engineered porous substrates must provide homogeneous water and nutrient distribution while maintaining sufficient aeration. To this aim, in (1) we set

$$\mathcal{J}(\mathbf{w}^{*,i}(\rho), \rho) = -\mathcal{D}(\rho), \quad \underline{c} = v_f, \quad \mathrm{C}(\mathbf{w}^{*,i}(\rho), \rho) = \mathcal{M}(\rho), \quad \overline{c} = 1, \tag{17}$$

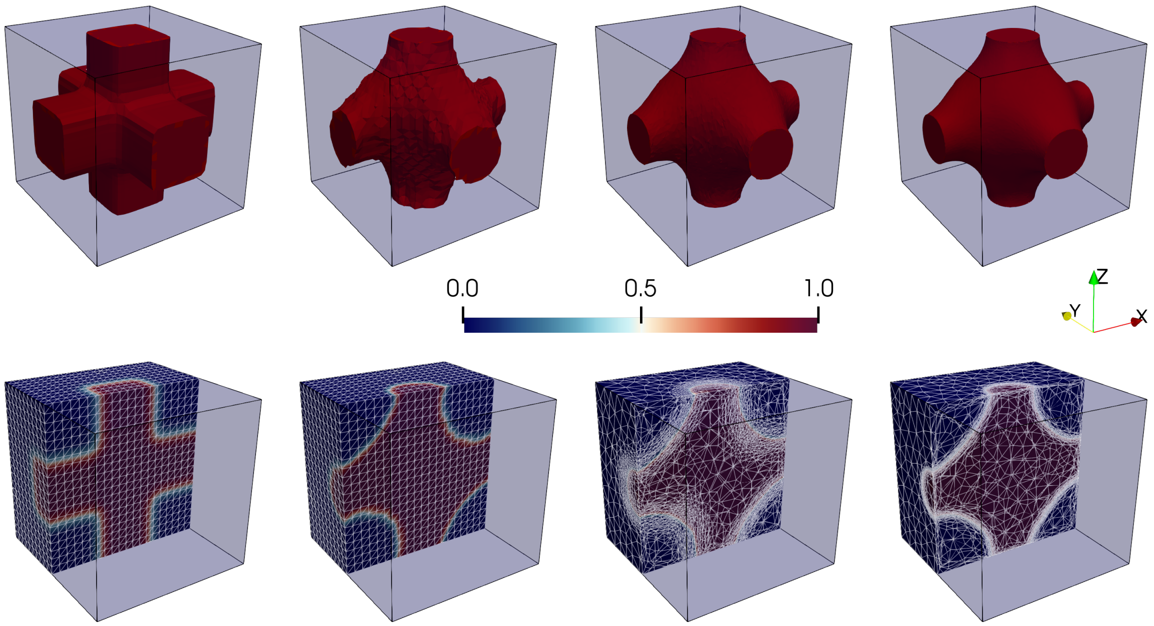

Figure 6: Design case $3_{0.3}$: density field (top) with the associated anisotropic adapted mesh overlapped (bottom) for {`iter`, `k` } = {0, 0}, {200, 0}, {300, 1}, {450, 7} (from left to right).

where $\mathbf{w}^{*,i}(\rho)$ are the state variables, solution to (15); the performance measure

$$\mathcal{D}(\rho) = \frac{k(\tilde{\rho})}{k_{\text{ref}}} \; - \; r_{\text{err}}\, \mathcal{E}(\tilde{\rho}), \tag{18}$$

inspired by [80, 81], which combines the isotropic (diagonal) permeability function

$$k(\tilde{\rho}) \;=\; \frac{1}{3}\sum_{i=1}^{3} K^H_{\tilde{\rho},ii},$$

with the anisotropic flow error

$$\mathcal{E}(\tilde{\rho}) = \frac{1}{k(\tilde{\rho})^2}\left[\sum_{ii,jj\in\{11,22,33\}} \frac{1}{2}(K^H_{\tilde{\rho},ii} - K^H_{\tilde{\rho},jj})^2 + \sum_{ij\in\{12,13,23\}} (K^H_{\tilde{\rho},ij})^2\right]$$

weighted by the reference value for the permeability $k_{\text{ref}}^{-1} = 10^3$ and $r_{\text{err}} \geq 0$, respectively, with $K^H_{\tilde{\rho},ij}$ the components of the homogenized permeability tensor $K^H_{\tilde{\rho}}$ defined as in (12) after replacing $\mathbf{w}^{*,i}$ with $\mathbf{w}^{*,i}(\rho)$; v_f and $\mathcal{M}(\rho)$ denote the volume fraction and the structure volume as in the previous sections. From a computational viewpoint, weight r_{err} is initially set to one and is gradually increased throughout the optimization iterations, so that early stages prioritize flow-channel discovery, while later iterations enforce isotropy more strictly.

The first investigation leads us to choose $v_f = 0.3$ and to identify the initial guess ρ_h^0 with a cross-shaped topology aligned with the Cartesian axes, coherently with the selected performance measure. The isotropic features requested in the optimization have a counterpart in the unit cell layout provided by `microSIMPATY` algorithm after `iter`$= 450$ (see Fig. 6 where notation Design $3_{0.3}$ is adopted for the output of this test case). Indeed, the optimizer consolidates a cross-like layout by smoothly rounding junctions and corners. Mesh adaptation concentrates resolution along the solid–void interface, accentuating the corner fillets and widening local bottlenecks. From a practical viewpoint, the obtained design allows us to reduce head losses and favor higher fluid velocities through the structure.

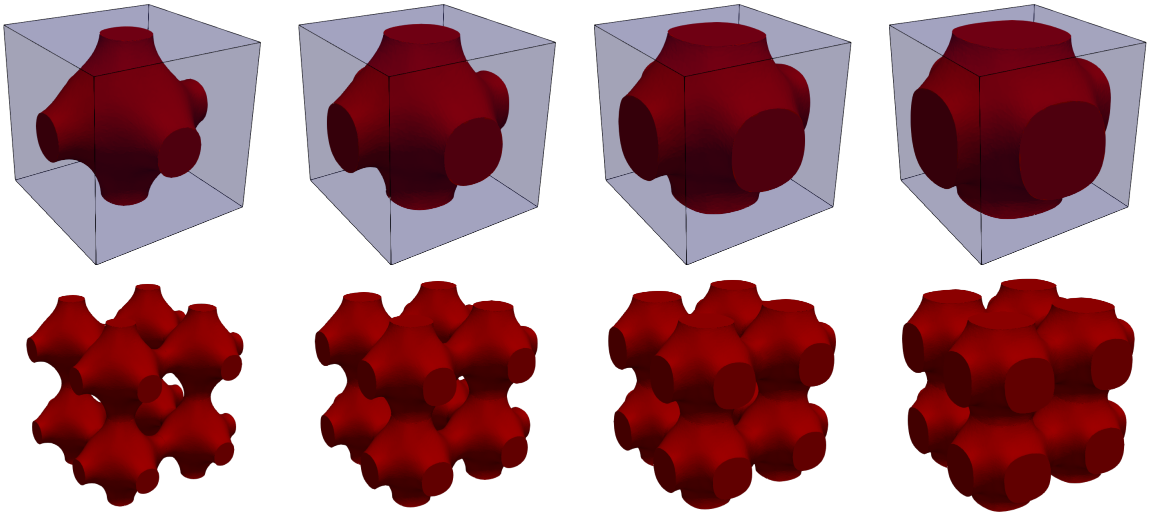

Figure 7: Design cases 3_{v_f}: unit cell (top) and associated $2\times2\times2$-layout cellular material (bottom), for $v_f \in \{0.3, 0.4, 0.5, 0.6\}$ (from left to right).

	$\mathcal{M}$	$10^{-2} \times k(\tilde{\rho})$	$10^{-5} \times \mathcal{E}(\tilde{\rho})$	$\#\mathcal{T}_h$	$s_{\max}$
Design case $3_{0.3}$					
$\underline{c}$	0.300	1.208	6.179	145199	160.672
C	0.300				
Design case $3_{0.4}$					
$\underline{c}$	0.400	0.723	6.627	167725	195.245
C	0.400				
Design case $3_{0.5}$					
$\underline{c}$	0.500	0.428	3.746	181822	208.961
C	0.500				
Design case $3_{0.6}$					
$\underline{c}$	0.600	0.242	0.4512	187753	270.695
C	0.600				

Table 3: Design cases 3_{v_f}: sensitivity analysis with respect to the volume fraction.

A sensitivity analysis with respect to the volume fraction is carried out varying $v_f \in$

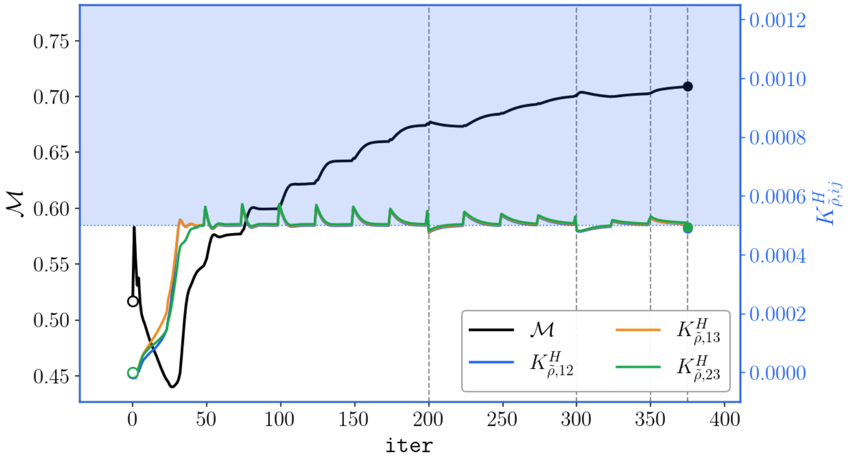

Figure 8: Design case $4_{0.0005}$: evolution of the objective functional $\mathcal{M}$ and of the constraints $K^H_{\tilde{\rho},ij}$ for $ij \in \{12, 13, 23\}$ as a function of `iter`. Mesh adaptation is applied in correspondence with the vertical dashed lines.

$\{0.3, 0.4, 0.5, 0.6\}$. Figure 7 compares the associated final design unit cells. The overall topology remains invariant across all configurations, where the geometry preserves a smooth, continuous shape that sustains efficient flow guidance. With increasing lower volume bounds, the core region thickens and corner curvatures become more pronounced, yielding a higher final cell volume. The $2 \times 2 \times 2$ tilings in the second row of the figure confirm the periodic consistency of the optimized layout whereas no internal void chambers develop, in accordance with permeability maximization under volume constraints. The values reported in Table 3 confirm the predominance of isotropic cell features. This is evident from the comparison between $k(\tilde{\rho})$ and $\mathcal{E}(\tilde{\rho})$, whose magnitudes differ by three orders, while the performance measure $\mathcal{D}$ in (18) reduces when v_f increases and vice versa. The volume constraint is strictly satisfied in all configurations, matching exactly the prescribed lower bound. Concerning the mesh adaptation step, the total number of elements increases with parameter v_f, consistently with the external surface growth that needs to be better resolved by the mesh.

3.2.2 Design case 4

This section focuses on the design of material layouts that promote diagonal flow within the xy, xz, and yz planes, while maximizing the allocation of the solid material. Such anisotropic fluid pathways are relevant for engineered lattices and corrugated-core architectures designed to guide flow preferentially along inclined directions, as required in multifunctional heat exchangers, drainage layers, or porous cooling panels [73, 74]. A similar design rationale is also valuable in soilless agriculture, where controlled drainage within porous substrates is crucial to maintain optimal moisture balance and root-zone aeration. This goal leads us to choose in (1)

$$\mathcal{J}(\mathbf{w}^{*,i}(\rho), \rho) = -\mathcal{M}(\rho), \quad \underline{\mathbf{c}} = [\underline{K}^H_{ij}], \quad \mathbf{C}(\mathbf{w}^{*,i}(\rho), \rho) = [K^H_{\tilde{\rho},ij}], \quad \overline{\mathbf{c}} = [10^{16}], \tag{19}$$

with $ij \in \{12, 13, 23\}$, where the coefficients $\underline{K}^H_{ij}$ set the lower admissible bounds for the constraints, whereas the value 10^{16} in $\overline{\mathbf{c}}$ effectively removes any limitation on the upper bound.

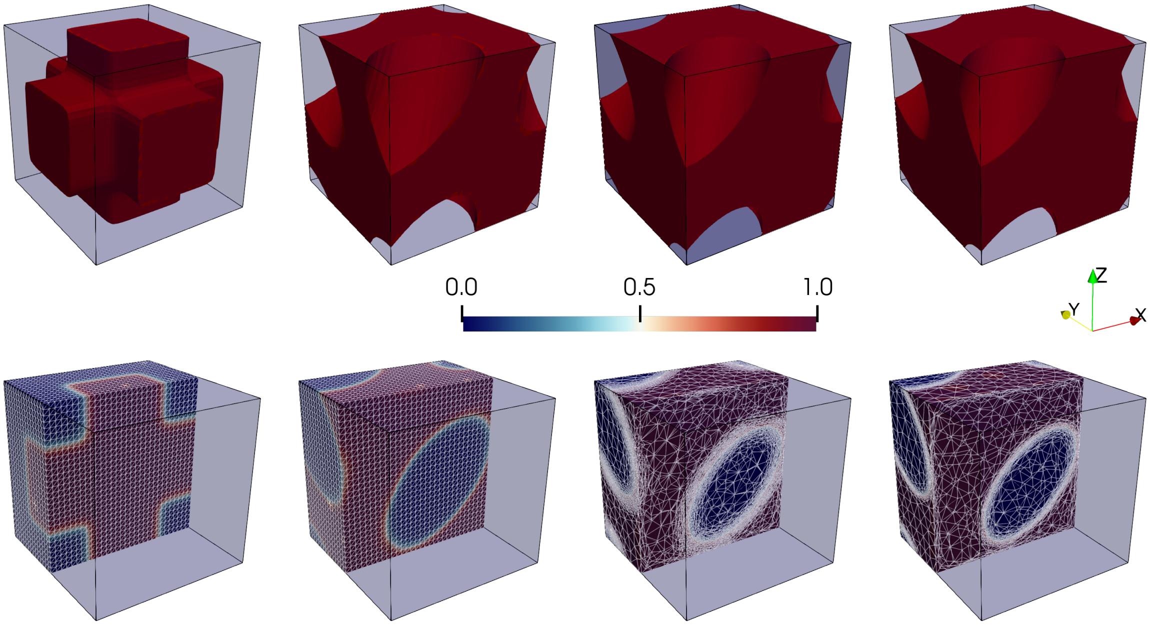

Figure 9: Design case $4_{0.0005}$: density field (top) with the associated anisotropic adapted mesh overlapped (bottom) for {`iter`, `k` } = {0, 0}, {200, 0}, {300, 1}, {375, 4} (from left to right).

As a first assessment, we consider a configuration characterized by a uniform lower bound $\underline{K}^H_{ij}$, set to 0.0005 for $ij \in \{12, 13, 23\}$. We refer to the associated design as to Design case $4_{0.0005}$. Identifying the initial guess with a cross-shaped topology as in Design Case 3, albeit with a different volume, the `miscroSIMPATY` algorithm drives the volume $\mathcal{M}$ to increase rapidly from the 30-th iteration, followed by a gradual approach toward stagnation. Conversely, after an initial transient phase, the constrained components of the homogenized permeability tensor remain close to $\underline{\mathbf{c}}$, exhibiting only mild oscillations (still to be ascribed to the variation of β) that are progressively damped throughout the iterations. Figure 8 exemplifies these remarks by displaying the evolution of $\mathcal{M}$ and of $K^H_{\tilde{\rho},12}$, $K^H_{\tilde{\rho},13}$, $K^H_{\tilde{\rho},23}$. As far as the unit cell layout is concerned, the optimizer thickens the material distribution along the three selected diagonal directions (see Fig. 9, top row), while the employment of an anisotropic adapted mesh (see Fig. 9, bottom row) rounds junctions, thus reducing head losses without violating the constraints.

By gradually increasing the uniform lower bound $\underline{K}^H_{ij}$ to 0.001 and 0.002, the `microSIMPATY` algorithm allocates less material, maintaining sufficiently conductive flow paths and largely preserving the characteristic diagonal-conducting topology (see Fig. 10, second and third columns). As a complementary check, we impose a non uniform lower bound for the selected homogenized permeability tensor components by setting $\underline{K}^H_{12} = 0.0015$, $\underline{K}^H_{13} = \underline{K}^H_{23} = 0.0005$. The resulting topology departs from the earlier symmetric configurations, though the dominant diagonal-flow orientation is still preserved (see Fig. 10, fourth column, where notation Design case $4_{0.0015,0.0005}$ is adopted for this configuration). Table 4 gathers the main quantities related to the `microSIMPATY` optimization process, for the four scenarios in Fig. 10. The final constraint values are very close to the prescribed lower bounds, and the required isotropy of the specimen is preserved across the first three settings, apart from minor fluctuations. As for the unit cell volume, a decrease in $\mathcal{M}$ is observed, in agreement with the trends reported in Fig. 10. On the contrary, the number of elements in the final adapted mesh increases, while the aspect ratio remains quite stable around 440.

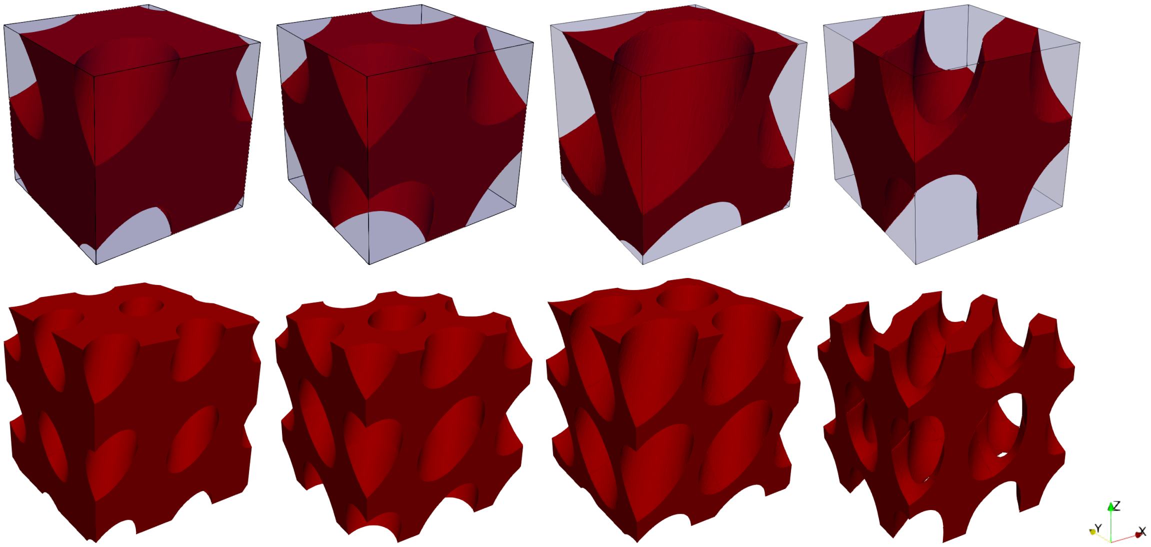

Figure 10: Design cases $4_{0.0005}$ (first column), $4_{0.001}$ (second column), $4_{0.002}$ (third column) and $4_{0.0015,0.0005}$ (fourth column): unit cell (top) and associated 2 × 2 × 2-layout cellular material (bottom).

	$10^{-4} \times K_{\tilde{\rho},12}$	$10^{-4} \times K_{\tilde{\rho},13}$	$10^{-4} \times K_{\tilde{\rho},23}$	$\mathcal{M}$	$\#\mathcal{T}_h$	$s_{\max}$
Design case $4_{0.0005}$						
$\underline{\mathbf{c}}$	5.0	5.0	5.0	0.723	157016	492.883
$\mathbf{C}$	5.038	5.038	5.038			
Design case $4_{0.001}$						
$\underline{\mathbf{c}}$	10.0	10.0	10.0.	0.649	172917	431.691
$\mathbf{C}$	10.057	10.058	10.057			
Design case $4_{0.002}$						
$\underline{\mathbf{c}}$	20.0	20.0	20.0	0.428	233089	478.206
$\mathbf{C}$	20.066	20.062	20.065			
Design case $4_{0.0015,0.0005}$						
$\underline{\mathbf{c}}$	15.0	5.0	5.0	0.4512	171700	367.783
$\mathbf{C}$	15.119	5.004	5.004			

Table 4: Design cases $4_{0.0005}$, $4_{0.001}$, $4_{0.002}$ and $4_{0.0015,0.0005}$: sensitivity analysis with respect to the lower bound for the permeability tensor components.

4 Multi-physics-constrained setting

Here, we extend the design framework introduced in (1) to a multi-physics setting, where the optimization is simultaneously driven by two distinct physical phenomena. Motivated by the target application of the paper and based on the findings from the previous analyses, we couple linear elasticity with Darcy–Stokes flow models, suitably adapting the optimization setting adopted so far.

It is to remark that, when coupling elasticity and fluid transport, the two objectives act, in general, antagonistically. As shown in the previous sections, enhancing elastic performance tends to increase mass and member thickness and may create enclosed void chambers to stiffen the cell. Conversely, meeting permeability requirements promotes open channels with preferred sizes and orientations, which generally reduce stiffness. Combining the two physics is therefore challenging, not only because of parameter tuning and potential infeasibilities, but also because the resulting designs trace a trade-off along a Pareto front.

Several studies have analyzed the maximization of the bulk modulus or permeability separately [81], typically resulting in nearly isotropic unit cells emphasizing either mechanical or fluid performance, depending on the chosen objective. In contrast, the present work aims to address both aspects concurrently to capture the intrinsic trade-off between structural stiffness and hydraulic conductivity. In particular, we simultaneously enforce shear-stiffness and diagonal-flow targets, merging the Design Cases 2 and 4. This multi-physics setting has practical relevance for the design of porous lattices employed in lightweight structural cores, heat exchangers, and bio-scaffolds, where mechanical support and directional fluid transport must coexist [73, 74]. This leads us to consider the multi-physics-constrained volume maximization setting

$$\min_{\rho\in R} -\mathcal{M}(\rho) \ : \begin{cases} \mathcal{A}_\rho(\mathbf{u}^{*,\,ij},\mathbf{v}) = \mathcal{F}_\rho(\mathbf{v}) \quad \forall \mathbf{v}\in V_\# \\ \mathbf{A}_\rho(\mathbf{U}(\rho),\mathbf{V}) = \mathbf{F}_\rho(\mathbf{V}) \quad \forall\mathbf{V}\in V_\#\times L^2_\#(\omega) \\ \underline{E}^G_{ijij} \le E^H_{\tilde{\rho},ijij} \ \le \ \overline{E}^G_{ijij} \\ K^H_{\tilde{\rho},ij} \ \ge \ \underline{K}^H_{ij} \\ \rho\in[\underline{\rho},1], \end{cases} \tag{20}$$

with $ij \in \{12, 13, 23\}$, where $\mathcal{A}_\rho$, $\mathcal{F}_\rho$, and $\mathbf{A}_\rho$, $\mathbf{F}_\rho$ are defined as in (7) and (15), respectively, while the constraints are the same as in Sections 3.1.2 and 3.2.2.

This optimization process can be interpreted from two complementary perspectives. In the first, starting from Design Case 2 with shear targets at minimum volume, selected permeability lower bounds $\underline{K}_{ij}$ are imposed, enforcing openings in regions that would otherwise remain sealed. In the second, starting from Design Case 4 with diagonal-flow bounds and volume maximization, some shear targets E^G_{ijij} are demanded to avoid excessively solid and thick configurations. In both cases, the volume maximization objective is retained to prevent the mechanical response from collapsing to its lower admissible limits.

Algorithm 1 is run starting from a spherical material initial guess ρ_h^0 and under the three optimization scenarios detailed in Table 5, where notation Design case $5_{E^G_{ijij},\underline{K}^H_{ij}}$ is adopted to distinguish the different configurations. The remaining input parameters to `microSIMPATY` are assigned as in Section 3.1. Figure 11 tracks the evolution of the volume $\mathcal{M}$ and of the six normalized constraints, associated with the setting in the first panel of the table. It is observed that the performance measure $\mathcal{M}$ exhibits a non-monotonic convergence history before reaching stagnation, whereas the constraints $E^H_{\tilde{\rho},ijij}$ and $K^H_{\tilde{\rho},ij}$ stabilize within only a few iterations. In particular, the former rapidly approach the associated upper bounds after the initial iterations, while the latter reach the corresponding lower bounds within the first 100 iterations and then gradually converge, consistently with the trend shown in Fig. 8 for the same quantities.

	$E^H_{\tilde{\rho},1212}$	$E^H_{\tilde{\rho},1313}$	$E^H_{\tilde{\rho},2323}$	$10^{-4} \times K^H_{\tilde{\rho},12}$	$10^{-4} \times K^H_{\tilde{\rho},13}$	$10^{-4} \times K^H_{\tilde{\rho},23}$	$\mathcal{M}$	$\#\mathcal{T}_h$	$s_{\max}$
Design case $5_{0.0577,0.0001}$									
$\underline{\mathbf{c}}$	0.0548	0.0548	0.0548	1.0	1.0	1.0	0.535	398839	588.178
$\mathbf{C}$	0.0606	0.0606	0.0606	1.013	1.012	1.014			
$\overline{\mathbf{c}}$	0.0606	0.0606	0.0606	10^{16}	10^{16}	10^{16}			
Design case $5_{0.0385,0.00015}$									
$\underline{\mathbf{c}}$	0.0365	0.0365	0.0365	1.5	1.5	1.5	0.418	253195	622.5
$\mathbf{C}$	0.0404	0.0404	0.0404	1.513	1.510	1.513			
$\overline{\mathbf{c}}$	0.0404	0.0404	0.0404	10^{16}	10^{16}	10^{16}			
Design case $5_{0.02503,0.0002}$									
$\underline{\mathbf{c}}$	0.0238	0.0238	0.0238	2.0	2.0	2.0	0.339	246258	533.753
$\mathbf{C}$	0.0239	0.0238	0.0239	2.012	2.012	2.011			
$\overline{\mathbf{c}}$	0.0263	0.0263	0.0263	10^{16}	10^{16}	10^{16}			

Table 5: Design cases $5_{0.0577,0.0001}$, $5_{0.0385,0.00015}$, $5_{0.02503,0.0002}$: sensitivity analysis with respect to the stiffness and permeability tensor components.

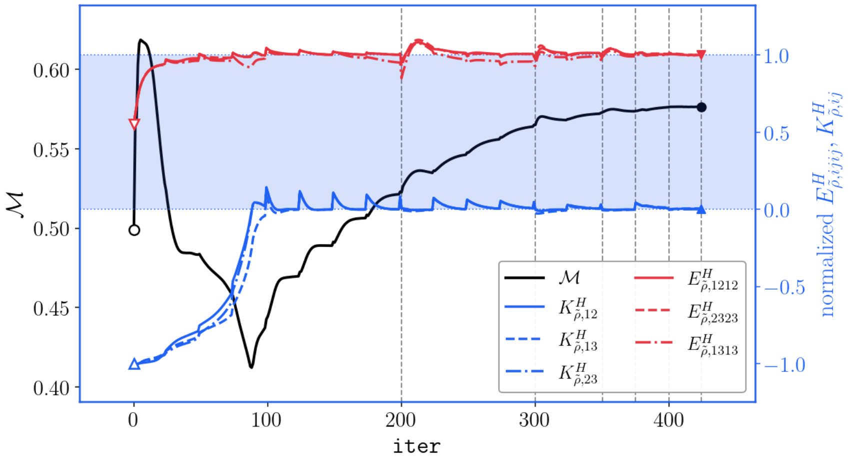

Figure 11: Design case $5_{0.0577,0.0001}$: evolution of the objective functional $\mathcal{M}$ and of the constraints $E^H_{\tilde{\rho},ijij}$ and $K^H_{\tilde{\rho},ij}$ for $ij \in \{12, 13, 23\}$ as a function of `iter`. Mesh adaptation is applied in correspondence with the vertical dashed lines.

Algorithm 1 stops at `iter` = 425, delivering a mesh consisting of 398839 tetrahedra, and produces the unit cell layout shown in the first column of Fig. 12. The resulting topology retains the diagonal-flow character observed in Design case 4, yet introduces openings and fissures. These additional features enhance fluid transport at the expense of elastic stiffness, as expected under competing physical constraints. This trade-off between mechanical and fluid requirements is further confirmed by the second and third panels of Table 5, where increased permeability must be balanced by milder targets on the components of the homogenized stiffness tensor to preserve problem feasibility. As a consequence, the material volume of the optimized unit cell decreases to accommodate more fluid, as clearly shown by the values of $\mathcal{M}$ in the table and by the cell layouts and $2 \times 2 \times 2$ tilings in Fig. 12.

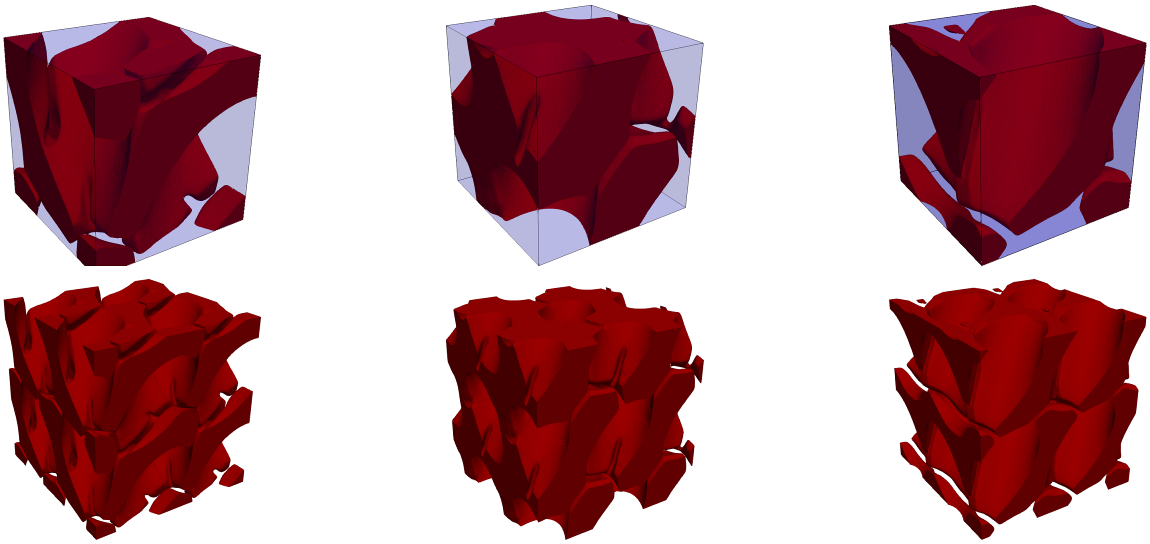

Figure 12: Design cases $5_{0.0577,0.0001}$ (first column), $5_{0.0385,0.00015}$ (second column), $5_{0.02503,0.0002}$ (third column): unit cell (top) and associated $2 \times 2 \times 2$-layout cellular material (bottom).

5 Design of new substrates for soilless cultivation

In soilless cultivation, the substrate must act as a scaffold that simultaneously provides structural support for plant growth and allows water and nutrients to reach the roots, enabling the proliferation throughout the growing medium. Design requirements for new substrates include the creation of an effective network of channels that prevents dead-ends and promotes root spreading, while ensuring isotropic pathways for uniform fluid transport even in the presence of cross-talk between channels. To support these objectives, the scaffold must resist transverse loads, maintaining mechanical stability relevant for root–substrate interactions, and provide through-channel connectivity along the Cartesian directions, so that roots grow upright and flow paths remain unimpeded without privileging a single direction. Thus, to support these objectives in the optimization problem formulation, we are led to properly bound the homogenized shear stiffness and Cartesian-directional permeability components.

With reference to the previous design cases, the requirement on the shear stiffness components remains consistent with Design case 2, while the promotion of fluid flow along preferred directions shifts from the diagonals, as in Design case 4, to the Cartesian axes. In accordance with the layout designs in Sections 3.2, it is also necessary to prevent degeneration into void-dominated configurations, leading to the identification of the performance measure as the maximization of volume. This corresponds to solve

$$\min_{\rho \in R} -\mathcal{M}(\rho) \ : \begin{cases} \mathcal{A}_\rho(\mathbf{u}^{*,\,ij}, \mathbf{v}) = \mathcal{F}_\rho(\mathbf{v}) \quad \forall \mathbf{v} \in V_\# \\ \mathbf{A}_\rho(\mathbf{U}(\rho), \mathbf{V}) = \mathbf{F}_\rho(\mathbf{V}) \quad \forall \mathbf{V} \in V_\# \times L^2_\#(\omega) \\ \underline{E}^G_{ijij} \leq E^H_{\tilde{\rho},ijij} \ \leq \ \overline{E}^G_{ijij} \\ K^H_{\tilde{\rho},\ell\ell} \ \geq \ \underline{K}^H_{\ell\ell} \\ \rho \in [\underline{\rho}, 1], \end{cases} \tag{21}$$

with $ij \in \{12, 13, 23\}$ and $\ell\ell = 11, 22, 33$, $\mathcal{A}_\rho$, $\mathcal{F}_\rho$, and $\mathbf{A}_\rho$, $\mathbf{F}_\rho$ defined as in (7) and (15), respectively.

	$E^H_{\tilde{\rho},1212}$	$E^H_{\tilde{\rho},1313}$	$E^H_{\tilde{\rho},2323}$	$10^{-2} \times K^H_{\tilde{\rho},11}$	$10^{-2} \times K^H_{\tilde{\rho},22}$	$10^{-2} \times K^H_{\tilde{\rho},33}$	$\mathcal{M}$	$\#\mathcal{T}_h$	$s_{\max}$
Design case SC$_1$									
$\underline{\mathbf{c}}$	0.0183	0.0183	0.0183	2.0	2.0	2.0	0.118	160022	71.254
$\mathbf{C}$	0.0184	0.0184	0.0185	2.021	2.021	2.021			
$\overline{\mathbf{c}}$	0.0202	0.0202	0.0202	10^{16}	10^{16}	10^{16}			
Design case SC$_2$									
$\underline{\mathbf{c}}$	0.0219	0.0219	0.0219	1.0	1.0	1.0	0.240	200416	117.580
$\mathbf{C}$	0.0242	0.0242	0.0242	1.013	1.013	1.012			
$\overline{\mathbf{c}}$	0.0242	0.0242	0.0242	10^{16}	10^{16}	10^{16}			
Design case SC$_3$									
$\underline{\mathbf{c}}$	0.0548	0.0548	0.0548	0.5	0.5	0.5	0.394	246268	70.096
$\mathbf{C}$	0.0548	0.0547	0.0547	0.5052	0.5051	0.5052			
$\overline{\mathbf{c}}$	0.0606	0.0606	0.0606	10^{16}	10^{16}	10^{16}			
Design case SC$_4$									
$\underline{\mathbf{c}}$	0.0219	0.0219	0.0219	1.0	1.0	0.5	0.276	213017	211.696
$\mathbf{C}$	0.0242	0.0241	0.0242	1.009	1.009	0.505			
$\overline{\mathbf{c}}$	0.0242	0.0242	0.0242	10^{16}	10^{16}	10^{16}			

Table 6: Design cases SC$_1$, SC$_2$, SC$_3$, SC$_4$: sensitivity analysis with respect to the stiffness and the permeability tensor components.

As a first experiment, we constrain the design process in (21) with the values in the second panel of Table 6, while setting the input parameters for `microSIMPATY` algorithm exactly as for the multi-physics framework in Section 4. The optimization converges at `iter`= 375, yielding the layout shown in the second column of Fig. 13, top row, here identified with the label SC$_2$. The material distribution satisfies the imposed constraints on the stiffness and permeability tensor components (see Table 6), forming diagonal structures (see Fig. 13, second column, center row) similar to those observed in Design case 2 and compliant with the prescribed shear bounds. At the same time, the unit cell exhibits additional void regions and narrow fissures, which provide more space for root growth and fluid motion. The effect of anisotropic mesh adaptation is evident in the smooth outer surfaces of the cell, provided by the refinement along the material/void interfaces and by the coarse tessellation in the internal regions.

With a view to prototyping scaffolds capable of hosting different cultivations with distinct growth requirements, we now explore the design space by varying the bounds of the constrained quantities (see Table 6). Specifically, we investigate: (i) the effects of lowering the shear stiffness target while increasing the minimum allowed diagonal permeability (Design case SC$_1$); (ii) the impact of higher mechanical targets combined with reduced substrate permeability demands

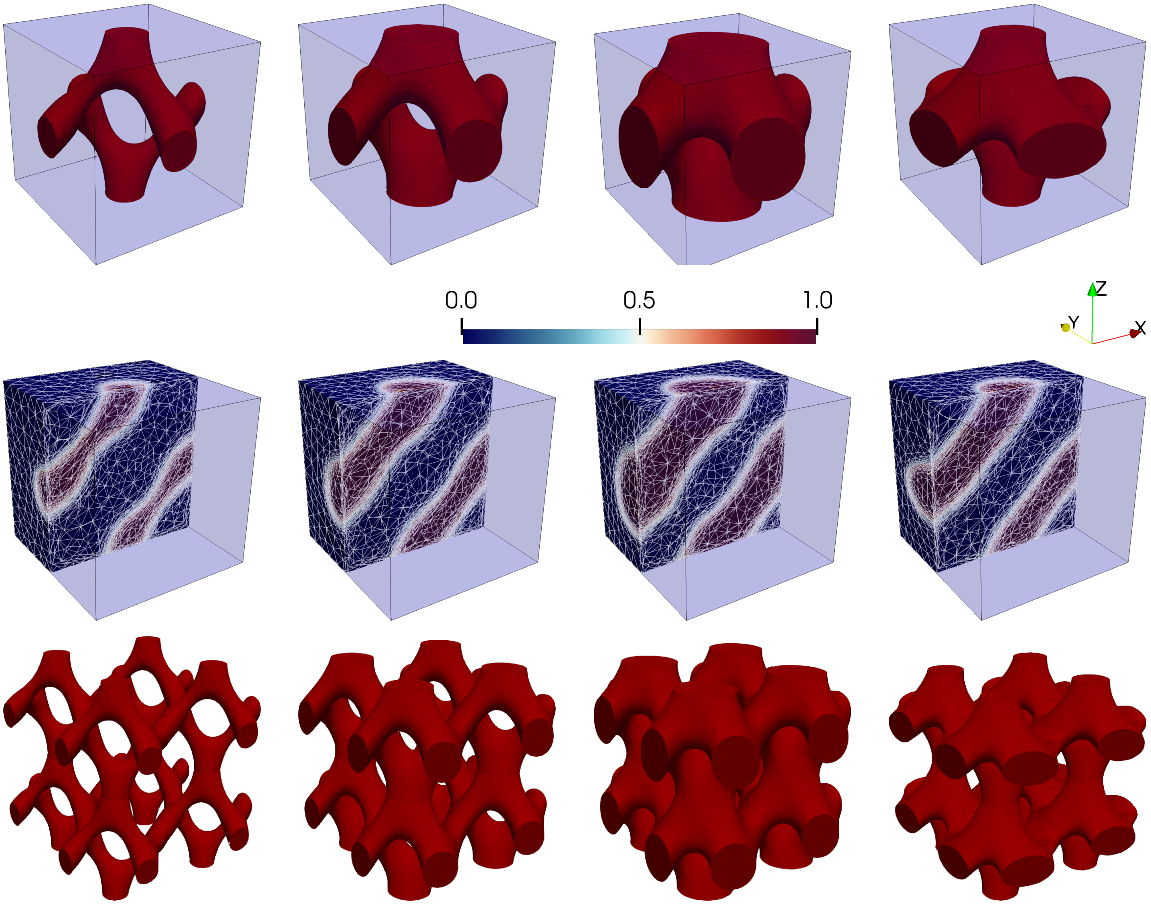

Figure 13: Design cases SC_i: unit cell (top) with the associated anisotropic adapted mesh overlapped (center) and associated $2 \times 2 \times 2$-layout cellular material (bottom), for $i = 1, \ldots, 4$ (from left to right).

(Design case SC_3); and (iii) the introduction of anisotropic permeability across the growth medium (Design case SC_4). As shown in Fig. 13, the scenario in (i) drives the design toward a more open, flow-friendly topology, whereas option (ii) acts in the opposite direction, producing thicker struts within the unit cell. The anisotropic requirement in (iii) is reflected in the asymmetric arrangement of the struts, with wider lateral channels that accommodate the higher permeability imposed along the lateral directions. The distinctive features of Design cases SC_1, SC_2, SC_3, and SC_4 are also evident in the views of the $2 \times 2 \times 2$ tiling shown in the figure. Finally, the values reported in Table 6 highlight that the elastic constraint is active and accommodates the requirements imposed by the two-sided inequality in (21), while the control over the fluidic properties promotes optimized values consistently close to the lower bound. From a computational standpoint, the adapted anisotropic mesh enables the management of a complex multiphysics optimization problem with a limited number of elements (within 250000 tetrahedra). It is observed that, in Design Case SC_4, the anisotropic permeability requirements have a corresponding effect on the maximum deformation value $s_{\max}$.

6 *In silico* study of substrates for in-vase growth

Building on the results presented in the previous section, we simulate crop development within the designed scaffolds. To assess the suitability of the optimized structures, we employ `RootBox` [84], an open-source `MATLAB` tool [85] that models plant root growth through an L-system–based approach [86]. In `RootBox`, a virtual pot can be defined to constrain the growth domain, allowing users to visualize how the root system develops within the container.

The standard version of `RootBox` supports only simple geometries (i.e., cylinders, truncated cones or parallelepipeds) defined by a small set of parameters. To enable the simulation of more complex containers, such as the cellular scaffolds considered in this manuscript, we extend the code to accept imported STL geometries. In particular, the distance from each container point to the scaffold surface is computed via an efficient `MATLAB` point-to-triangle distance algorithm, which returns the minimum distance between the point and the triangular facets of the scaffold mesh. Furthermore, to support *in silico* studies of plant growth in soilless cultivation systems, we implemented a bounding-box correction that prevents roots from escaping the scaffold domain. This particulare configuration aims to reproduce standard nurseries used for germination, in which multiple slots are embedded within a larger container. These enhancements extend the flexibility of `RootBox`, enabling its application to a broad range of growth scenarios.

parameter	definition	mean value	standard deviation
		Primary root	
`r`	growth rate	3.0 [cm/day]	–
`lb`	basal zone length	0.7 [cm]	–
`la`	apical zone length	1.0 [cm]	–
`ln`	length between laterals	0.37 [cm]	0.25 [cm]
`nob`	maximum number of laterals	540	–
`a`	root radius	0.015 [cm]	–
`theta`	insertion angle	0.0	–
`dx`	step length	0.25 [cm]	–
`successor`	number of successors	2	–
`tropism`	tropism	$[1, 5, \pi/9]$	–
		Lateral roots	
`r`	growth rate	0.57 [cm/day]	–
`la`	apical zone length	200 [cm]	–
`ln`	length between laterals	0.37 [cm]	0.25 [cm]
`a`	root radius	0.012 [cm]	–
`theta`	insertion angle	$7\pi/18$	$\pi/9$
`dx`	step length	0.25 [cm]	–
`tropism`	tropism	$[1, 1, \pi/9]$	–

Table 7: *In silico* growth: input parameters for rapeseed used in `RootBox` (the standard deviation is null when not specified).

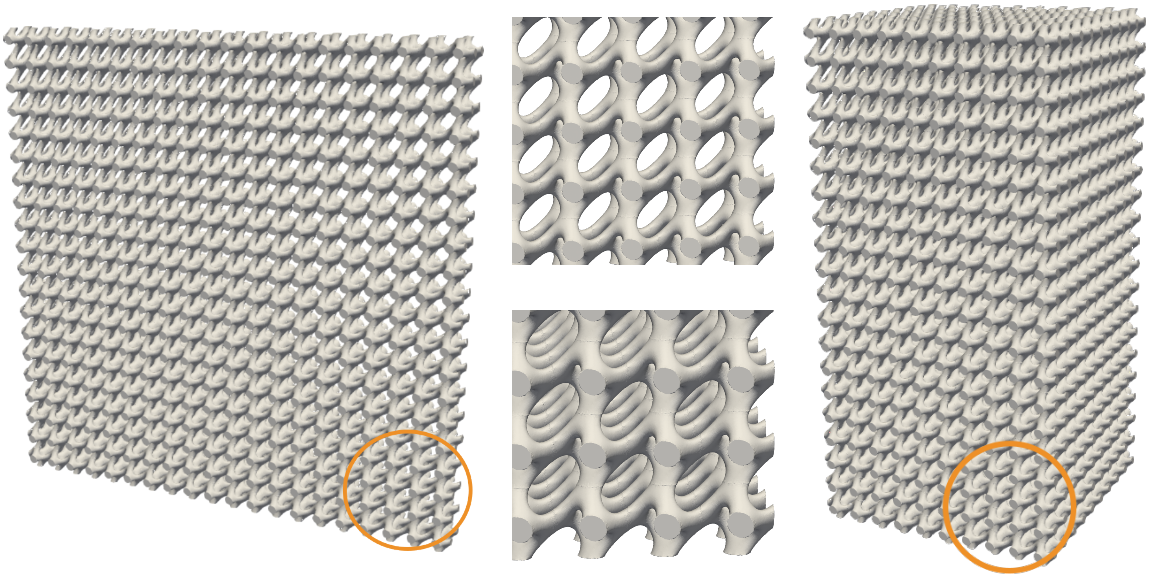

Figure 14: *In silico* growth: rhizotron-like (left) and parallelepiped vase (right) containers; close-up view of the constituting cellular structures in correspondence of the highlighted circled area (center) for the rhizotron (top) and the vase (bottom) configurations.

To assess the innovative scaffold designs, we consider two virtual containers, namely a rhizotron-like and a parallelepiped vase, both constructed by periodically repeating the unit cell of Design case SC_2 in Fig. 13. The scaffolded structures are reported in Fig. 14, left and right. This preliminary investigation aims to explore the ability of this design case to support complex root architectures, considering its potential balance between permeability, mechanical strength, and geometric versatility.

For the specific crop, we select rapeseed, a flowering member of the *Brassicaceae* family, due to the compatibility between seed and root sizes and the dimensions of the scaffold unit cells. Table 7 summarizes the main parameters and corresponding values (randomized according to given mean value and standard deviation) governing both primary and lateral root growth for this crop, as defined in the script `Example_Rhizotron.m` provided with `RootBox`. Here, gravity is assumed as the primary driver of growth direction over a 20-day simulation period.

Rhizotron configuration A rhizotron is a permanent installation designed to study subsurface phenomena such as root development. Typically, it consists of a thin slab of undisturbed native soil enclosed within a transparent container [87]. A common geometric representation is a thin parallelepiped with a small depth, which is generally filled with soil or, as in the novel soilless agriculture-oriented configuration proposed here, with a periodic repetition of the unit cell SC_2. In this study, we model a cellular structure with dimensions $L_x = 10$ [cm], $L_y = 1$ [cm], and $L_z = 10$ [cm], where each unit cell has a side length of 0.5 [cm] (see Fig. 14, left and top-center).

The 20-day period is split into 300 time-frames. The three panels in Fig. 15 (top and bottom-left) illustrate the evolution of primary and lateral roots at frame 100, 150 and 300. A clear downward growth of the primary root can be observed under the effect of gravitropism, whereas the lateral roots initially expand horizontally and subsequently exhibit a more irregular upward development. This behavior is mainly constrained by the presence of the internal cellular structure and the confining walls of the rhizotron.

For comparison, we repeated the simulation using native soil instead of the cellular scaffold. As shown in the bottom-right panel of Fig. 15, the primary root displays a smoother, less tortuous growth pattern, likely due to the absence of the internal obstacles provided by the lattice. This results in an accumulation of the roots at the bottom, whereas the presence of a scaffold provides anchoring points for both the primary and lateral roots, thereby increasing the root surface area available for water and nutrient exchange.

Vase configuration In a second validation test, we examine root development within a vase-like container configuration. This setup represents a standard environment for cultivation. The modeled structure has dimensions $L_x = L_y = 5$ [cm] and $L_z = 10$ [cm], and is filled through the periodic repetition of the same unit cell SC_2 as in the rhizotron case, with the same time 20-day period and 300 time-frames. The resulting geometry is shown in Fig. 14 (right and center-bottom for a detail). Figure 16 (top and bottom-left panels) displays the simulated trajectories of primary and lateral roots at frame 100, 150 and 300. The primary root initially follows a predominantly vertical downward path (top-left), taking advantage of the larger vertical dimension of the container. As growth progresses, the trajectory gradually transitions to a more horizontal pattern (top-right), with a noticeable accumulation of roots near the bottom region (bottom-left). The lateral roots, in turn, exhibit an increasingly invasive development, expanding the spatial distribution concurrently with the elongation of the primary root system.

The response of root organization to the replacement of native soil with a cellular scaffold is analyzed in the vase configuration, analogously to the rhizotron case. A comparison of the bottom panels in Fig. 16 indicates that, in the soil-only case, the primary root follows an undisturbed vertical growth before spreading horizontally at the base, while lateral roots predominantly develop upward from the bottom region. When the cellular structure is introduced, the primary root trajectory becomes perturbed, and lateral root expansion shifts toward the horizontal plane, leading to a reduced presence in the central and upper zones of the domain.

7 Conclusions and future developments

In this work, we demonstrated that the design pipeline for cellular materials driven by the `microSIMPATY` algorithm can be effectively employed in the framework of soilless agriculture, enabling the replacement of conventional cultivation media with engineered cellular scaffolds. This approach is instrumental to support the synthesis of substrate architectures with enhanced sustainability, reduced production costs, and the potential for local, automated, and controlled manufacturing.

The fully three-dimensional extension of `microSIMPATY` retains the benefits of the original 2D version, including minimal density filtering, sharp solid–void interface resolution, reduced post-processing, and a largely automated workflow, while offering great flexibility to meet diverse design objectives. Specifically, we showed how different combinations of objective and constraint sets (e.g., bulk-modulus maximization under volume constraints, shear-stiffness enhancement at minimum volume, isotropic permeability promotion, and diagonal-flow control) lead to distinct and physically interpretable unit cell topologies across both single- and multi-physics settings governed by homogenized linear elasticity and Darcy–Stokes flow models.
This versatile framework proved instrumental for developing potential soil surrogates capable of providing mechanical support while promoting isotropic water and nutrient transport. The

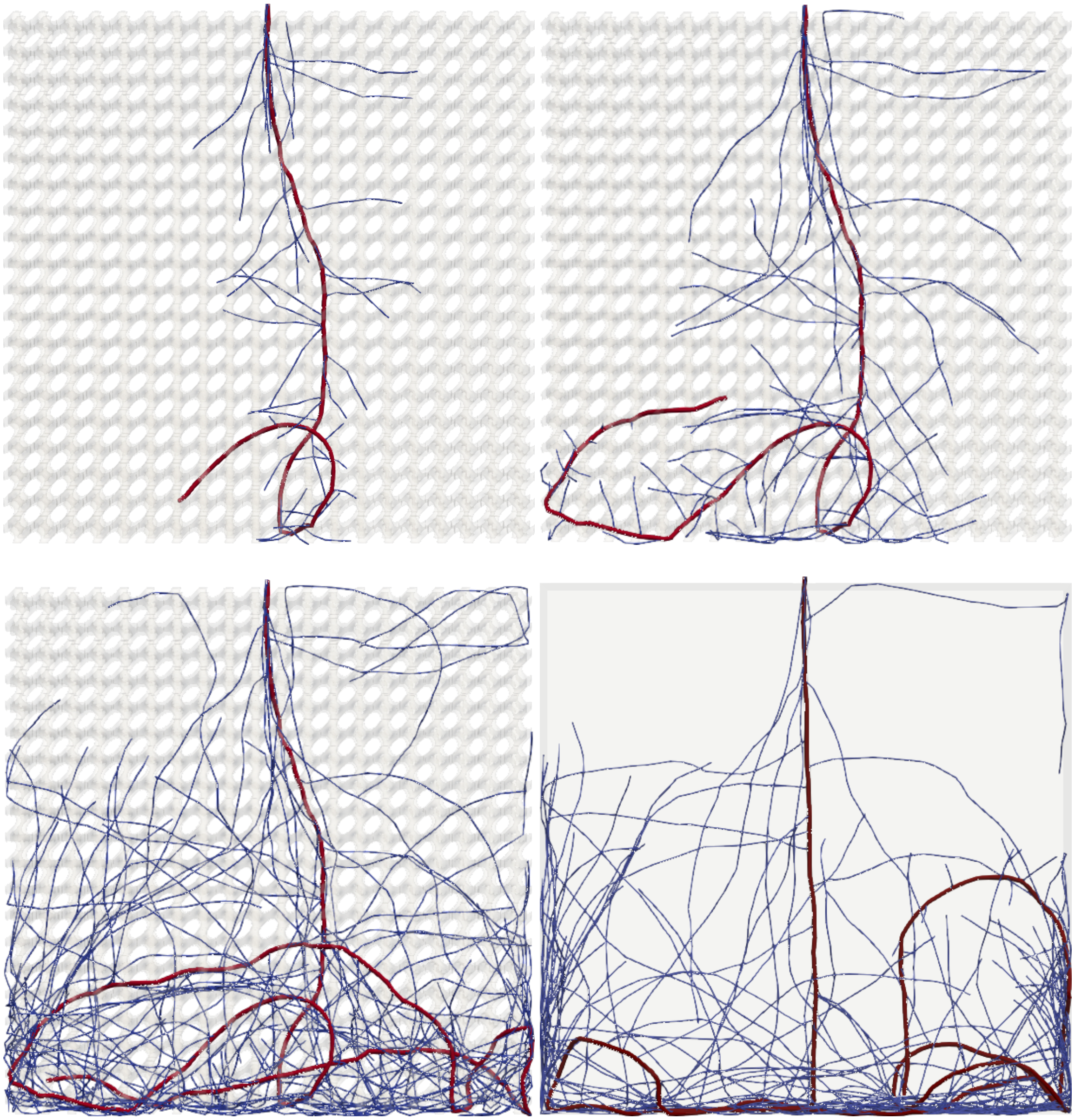

Figure 15: *In silico* growth – rhizotron configuration: distribution of the primary and lateral roots at frame 100 (top-left), 150 (top-right) and 300 (bottom-left) for the scaffolded container and at frame 300 for the standard native soil setting (bottom-right).

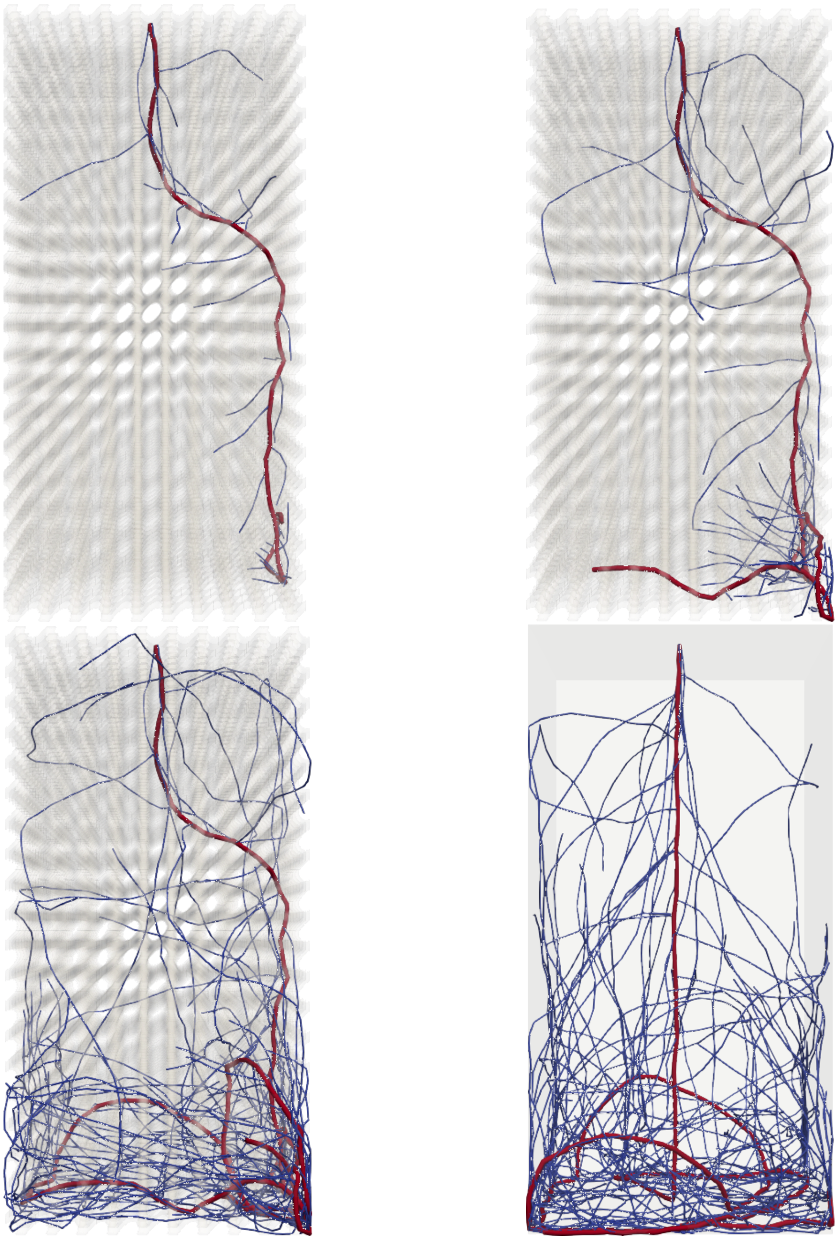

Figure 16: *In silico* growth – vase configuration: distribution of the primary and lateral roots at frame 100 (top-left), 150 (top-right) and 300 (bottom-left) for the scaffolded container and at frame 300 for the standard native soil setting (bottom-right).

`RootBox` platform has been extended to perform *in silico* root-growth simulations within the optimized cellular scaffolds, qualitatively validating the capability to host root systems.

For the practical implementation of the proposed pipeline for the advanced substrate design, additional properties critical for soilless cultivation must be considered in the optimization process, such as water retention and capillarity, salinity accumulation and flushing cycles, cleanability for reuse. Equally essential are the manufacturability of these scaffolds and the selection of suitable materials for the fabrication. At present, a preliminary manufacturing phase has been undertaken, in which a scaffold based on the SC_2 design has been 3D printed using PLA, chosen for the compostable and biodegradable properties. Scaling up to realistic, larger configurations is ultimately pivotal for *in vivo* testing. In this regard, a collaboration has already been successfully established with the Department of Agricultural and Environmental Sciences at the University of Milan.

Acknowledgments

G.S., N.M, N.F. and S.P. are members of the Gruppo Nazionale Calcolo Scientifico Istituto Nazionale di Alta Matematica (GNCS–INdAM). N.F. and S.P. acknowledge the INdAM-GNCS 2025 project "Modelli Matematici Supportati dall'Integrazione di Dati per Agricoltura Sostenibile". G.S., N.M, and S.P. acknowledge the support by MUR, grant Dipartimento di Eccellenza 2023–2027.

References

[1] Kyle F. Davis et al. "Meeting future food demand with current agricultural resources". In: *Global Environ. Change* 39 (2016), pp. 125–132.

[2] FAO. *How to Feed the World in 2050.* Tech. rep. Food and Agriculture Organization, 2009.

[3] Bojana Bajželj et al. "Importance of food-demand management for climate mitigation". In: *Nat. Clim. Change* 4.10 (2014), pp. 924–929.

[4] Chantal Le Mouël and Agneta Forslund. "How can we feed the world in 2050? A review of the responses from global scenario studies". In: *Eur. Rev. Agric. Econ.* 44.4 (2017), pp. 541–591.

[5] David Satterthwaite, Gordon McGranahan, and Cecilia Tacoli. "Urbanization and its implications for food and farming". In: *Philos. Trans. R. Soc. Lond. B Biol. Sci.* 365.1554 (2010), pp. 2809–2820.

[6] Chao Yuan et al. "Effects of vertical farming on natural ventilation of residential buildings". In: *Energy Build.* 185 (2019), pp. 316–325.

[7] M. Raviv and J. H. Lieth. "Significance of Soilless Culture in Agriculture". In: *Soilless Culture – Theory and Practice.* Amsterdam: Elsevier, 2008, pp. 1–11.

[8] K. A. El-Kazzaz and A. A. El-Kazzaz. "Soilless agriculture: a new and advanced method for agriculture development – An introduction". In: *Agric. Res. Technol. Open Access J.* 3 (2017), pp. 63–72.

[9] Yahia Othman et al. "Soilless culture: Management of growing substrate, water, nutrient, salinity, microorganism and product quality". In: *Fresen. Environ. Bull.* 28.4 (2019), pp. 3249–3260.

[10] P Agung Putra and Henry Yuliando. “Soilless culture system to support water use efficiency and product quality: A review”. In: *Agric. Agric. Sci. Procedia* 3 (2015), pp. 283–288.

[11] P. Gopinath, P. Irene Vethamoni, and M. Gomathi. “Aeroponics soilless cultivation system for vegetable crops”. In: *Chem. Sci. Rev. Lett.* 6.22 (2017), pp. 838–849.

[12] Imran Ali Lakhiar et al. “Modern plant cultivation technologies in agriculture under controlled environment: A review on aeroponics”. In: *J. Plant Interact.* 13.1 (2018), pp. 338–352.

[13] Roberto S. Velazquez-Gonzalez et al. “A review on hydroponics and the technologies associated for medium- and small-scale operations”. In: *Agriculture* 12.5 (2022), p. 646.

[14] A Rodríguez-Delfín. “Advances of hydroponics in Latin America”. In: *II International Symposium on Soilless Culture and Hydroponics.* Vol. 947. 2011, pp. 23–32.

[15] L. I. Inisheva. “Peat soils: genesis and classification”. In: *Eurasian Soil Sci.* 39 (2006), pp. 699–704.

[16] Giuliana Vinci and Mattia Rapa. “Hydroponic cultivation: Life cycle assessment of substrate choice”. In: *Br. Food J.* 121.8 (2019), pp. 1801–1812.

[17] Th. G. L. Aendekerk et al. *International Substrate Manual: Analysis, Characteristics, Recommendations.* Amsterdam: Elsevier, 2000.

[18] Dennis Dannehl et al. “Evaluation of substitutes for rock wool as growing substrate for hydroponic tomato production”. In: *J. Appl. Bot. Food Qual* 88 (2015), pp. 68–77.

[19] WT Bussell and S Mckennie. “Rockwool in horticulture, and its importance and sustainable use in New Zealand”. In: *N. Z. J. Crop Hortic. Sci.* 32.1 (2004), pp. 29–37.

[20] Livia M. Kalossaka et al. “3D printing hydrogels for the fabrication of soilless cultivation substrates”. In: *Appl. Mater. Today* 24 (2021), p. 101088.

[21] Xiaoxue Jia et al. “Chitin and chitosan: Pioneering sustainable substrates for next-generation soilless vertical farming”. In: *Trends Food Sci. Technol.* 150 (2024), p. 104599.

[22] N. Ferro et al. “Design of cellular materials for multiscale topology optimization: application to patient-specific orthopedic devices”. In: *Struct. Multidiscip. Optim.* 65.3 (2022), p. 79.

[23] N. Ferro et al. “Designing novel vascular stents with enhanced mechanical behavior through topology optimization of existing devices”. In: *Finite Elem. Anal. Des.* 244 (2025), p. 104304.

[24] Wei Tao et al. “Multi-scale design of three dimensional woven composite automobile fender using modified particle swarm optimization algorithm”. In: *Compos. Struct.* 181 (2017), pp. 73–83.

[25] Max MJ Opgenoord and Karen E Willcox. “Design for additive manufacturing: cellular structures in early-stage aerospace design”. In: *Struct. Multidiscip. Optim.* 60.2 (2019), pp. 411–428.

[26] J. S. Rao et al. “Topology optimization of aircraft wing”. In: *J. Aerosp. Sci. Technol.* 61.3 (2009), pp. 402–414.

[27] Stefano Soprani et al. “A design approach for integrating thermoelectric devices using topology optimization”. In: *Appl. Energy* 176 (2016), pp. 49–64.

[28] M.P. Bendsøe. “Optimal Shape Design as a Material Distribution Problem”. In: *Struct. Optim.* 1.4 (1989), pp. 193–202.

[29] G. Allaire, F. Jouve, and A.M. Toader. “A Level Set Method for Structural Optimization”. In: *Comput. Mech.* 31.3 (2002), pp. 189–204.

[30] Julian A Norato et al. “A topological derivative method for topology optimization”. In: *Struct. Multidiscip. Optim.* 33 (2007), pp. 375–386.

[31] B. Bourdin and A. Chambolle. “Design of Structures with Phase-Field Models”. In: *J. Comput. Phys.* 173.2 (2003), pp. 720–741.

[32] Y.M. Xie and G.P. Steven. “A Simple Evolutionary Procedure for Structural Optimization”. In: *Comput. Struct.* 49.5 (1993), pp. 885–896.

[33] E. Andreassen and C.S. Andreasen. “How to determine composite material properties using numerical homogenization”. In: *Comput. Mater. Sci.* 83 (2014), pp. 488–495.

[34] O. Sigmund. “Materials with prescribed constitutive parameters: an inverse homogenization problem”. In: *Int. J. Solids Struct.* 31.17 (1994), pp. 2313–2329.

[35] N. Ferro, S. Micheletti, and S. Perotto. “Density-based inverse homogenization with anisotropically adapted elements”. In: *Numerical Methods for Flows.* Vol. 132. Lect. Notes Comput. Sci. Eng. Cham: Springer International Publishing, 2020, pp. 211–221.

[36] S. Micheletti and S. Perotto. “Anisotropic adaptation via a Zienkiewicz–Zhu error estimator for 2D elliptic problems”. In: *Numerical Mathematics and Advanced Applications.* Springer Berlin, Heidelberg. 2010, pp. 645–653.

[37] D. Carbonaro et al. “Design of innovative self-expandable femoral stents using inverse homogenization topology optimization”. In: *Comput. Methods Appl. Mech. Eng.* 416 (2023), p. 116288.

[38] M. Gavazzoni et al. “Multi-Physics Inverse Homogenization for the Design of Innovative Cellular Materials: Application to Thermo-Elastic Problems”. In: *Math. Comput. Appl.* 27.15 (2022).

[39] G. Speroni and N. Ferro. *A novel metric-based mesh adaptation algorithm for 3D periodic domains.* Tech. rep. 61. MOX Report - Politecnico di Milano, Dipartimento di Matematica, 2024.

[40] Grégoire Allaire. “Homogenization and two-scale convergence”. In: *SIAM J. Math. Anal.* 23.6 (1992), pp. 1482–1518.

[41] Enrique Sánchez-Palencia. *Non-Homogeneous Media and Vibration Theory.* Vol. 127. Lecture Notes in Physics. Berlin: Springer, 1980.

[42] Fermin Otero, Sergio Oller, and Xavier Martinez. “Multiscale computational homogenization: Review and proposal of a new enhanced-first-order method”. In: *Arch. Comput. Methods Eng.* 25 (2018), pp. 479–505.

[43] Niclas Strömberg. “A new multi-scale topology optimization framework for optimal combinations of macro-layouts and local gradings of TPMS-based lattice structures”. In: *Mech. Based Des. Struct. Mach.* 52.1 (2024), pp. 257–274.

[44] Patrick S Chang and David W Rosen. “The size matching and scaling method: a synthesis method for the design of mesoscale cellular structures”. In: *Int. J. Comput. Integr. Manuf.* 26.10 (2013), pp. 907–927.

[45] Jason Nguyen, Sang-in Park, and David Rosen. “Heuristic optimization method for cellular structure design of light weight components”. In: *Int. J. Precis. Eng. Manuf.* 14.6 (2013), pp. 1071–1078.

[46] Martin P. Bendsøe and Ole Sigmund. *Topology Optimization: Theory, Methods, and Applications*. Berlin, Heidelberg: Springer-Verlag, 2003.

[47] A. Ern and J. L. Guermond. *Theory and Practice of Finite Elements*. Vol. 159. New York, NY: Springer, 2004.

[48] JoséMiranda Guedes and Noboru Kikuchi. “Preprocessing and postprocessing for materials based on the homogenization method with adaptive finite element methods”. In: *Comput. Methods Appl. Mech. Eng.* 83.2 (1990), pp. 143–198.

[49] Guoying Dong, Yunlong Tang, and Yaoyao Fiona Zhao. “A 149 line homogenization code for three-dimensional cellular materials written in MATLAB”. In: *J. Eng. Mater. Technol.* 141.1 (2019), p. 011005.

[50] O. Sigmund and J. Petersson. “Numerical instabilities in topology optimization: a survey on procedures dealing with checkerboards, mesh-dependencies and local minima”. In: *Struct. Multidisc. Optim.* 16.1 (1998), pp. 68–75.

[51] Ole Sigmund. “Manufacturing tolerant topology optimization”. In: *Acta Mech. Sin.* 25.2 (2009), pp. 227–239.

[52] Fengwen Wang, Boyan Stefanov Lazarov, and Ole Sigmund. “On projection methods, convergence and robust formulations in topology optimization”. In: *Struct. Multidiscip. Optim.* 43.6 (2011), pp. 767–784.

[53] Jeroen P Groen et al. “Higher-order multi-resolution topology optimization using the finite cell method”. In: *Int. J. Numer. Methods Eng.* 110.10 (2017), pp. 903–920.

[54] Markus J Geiss and Kurt Maute. “Topology optimization of active structures using a higher-order level-set-XFEM-density approach”. In: *2018 Multidisciplinary analysis and optimization conference*. AIAA AVIATION Forum AIAA 2018-4053. 2018, pp. 1–13.

[55] Kristian Ejlebjerg Jensen. “Anisotropic mesh adaptation and topology optimization in three dimensions”. In: *J. Mech. Des.* 138.6 (2016), p. 061401.

[56] S. Micheletti, S. Perotto, and L. Soli. “Topology optimization driven by anisotropic mesh adaptation: Towards a free-form design”. In: *Comput. Struct.* 214 (2019), pp. 60–72.

[57] Krister Svanberg. “The method of moving asymptotes—a new method for structural optimization”. In: *Int. J. Numer. Methods Eng.* 24.2 (1987), pp. 359–373.

[58] Krister Svanberg. *MMA and GCMMA — Two Methods for Nonlinear Optimization.* Tech. rep. KTH Royal Institute of Technology, Department of Mathematics, 2007.

[59] Boyan Stefanov Lazarov and Ole Sigmund. “Filters in topology optimization based on Helmholtz-type differential equations”. In: *Int. J. Numer. Methods Eng.* 86.6 (2011), pp. 765–781.

[60] D. Cortellessa et al. “Enhancing level set-based topology optimization with anisotropic graded meshes”. In: *Appl. Math. Comput.* 447 (2023), p. 127903.

[61] P. L. George et al. “Mesh Generation and Mesh Adaptivity: Theory and Techniques”. In: *Encyclopedia of Computational Mechanics*. Chichester, UK: John Wiley & Sons, Ltd, 2007. Chap. 17, pp. 1–31.

[62] P.J. Frey and F. Alauzet. “Anisotropic mesh adaptation for CFD computations”. In: *Comput. Methods Appl. Mech. Eng.* 194.48 (2005), pp. 5068–5082.

[63] O. C. Zienkiewicz and J. Z. Zhu. “The superconvergent patch recovery and a posteriori error estimates. Part 1: The recovery technique”. In: *Int. J. Numer. Methods Eng.* 33.7 (1992), pp. 1331–1364.

[64] O. C. Zienkiewicz and J. Z. Zhu. “The superconvergent patch recovery and a posteriori error estimates. Part 2: Error estimates and adaptivity”. In: *Int. J. Numer. Methods Eng.* 33.7 (1992), pp. 1365–1382.

[65] P.E. Farrell, S. Micheletti, and S. Perotto. “An anisotropic Zienkiewicz–Zhu-type error estimator for 3D applications”. In: *Int. J. Numer. Methods Eng.* 85.6 (2011), pp. 671–692.

[66] F. Hecht. “New development in FreeFem++”. In: *J. Numer. Math.* 20.3-4 (2012), pp. 251–266.

[67] The FEniCS Project. *DOLFINx Python Documentation, Version 0.10.0.post0.* 2024. URL: `https://docs.fenicsproject.org/dolfinx/v0.10.0.post0/python/index.html`.

[68] Lisandro D. Dalcin et al. “Parallel distributed computing using Python”. In: *Adv. Water Resour.* 34.9 (2011), pp. 1124–1139.

[69] Mmg Platform Team. *Mmg: Open-Source Anisotropic and Isotropic Mesh Adaptation Platform.* 2025. URL: `https://www.mmgtools.org/`.

[70] Peter Helnwein. “Some remarks on the compressed matrix representation of symmetric second-order and fourth-order tensors”. In: *Comput. Methods Appl. Mech. Eng.* 190.22–23 (2001), pp. 2753–2770.

[71] Martin P Bendsøe and Ole Sigmund. “Material interpolation schemes in topology optimization”. In: *Arch. Appl. Mech.* 69.9 (1999), pp. 635–654.

[72] Zvi Hashin and Shmuel Shtrikman. “A variational approach to the theory of the elastic behaviour of multiphase materials”. In: *J. Mech. Phys. Solids.* 11.2 (1963), pp. 127–140.

[73] Anthony G Evans et al. "The topological design of multifunctional cellular metals". In: *Prog. Mater. Sci.* 46.3-4 (2001), pp. 309–327.

[74] Haydn NG Wadley. "Multifunctional periodic cellular metals". In: *Philos. Trans. R. Soc. A* 364.1838 (2006), pp. 31–68.

[75] Robert G Hutchinson and Norman A Fleck. "The structural performance of the periodic truss". In: *J. Mech. Phys. Solids* 54.4 (2006), pp. 756–782.

[76] Mark C Messner. "Optimal lattice-structured materials". In: *J. Mech. Phys. Solids* 96 (2016), pp. 162–183.

[77] Thomas Borrvall and Joakim Petersson. "Topology optimization of fluids in Stokes flow". In: *Int. J. Numer. Methods Fluids* 41.1 (2003), pp. 77–107.

[78] D. Boffi, F. Brezzi, and M. Fortin. *Mixed Finite Element Methods and Applications.* Vol. 44. Heidelberg: Springer Berlin, 2013.

[79] Arif Masud and Thomas JR Hughes. "A stabilized mixed finite element method for Darcy flow". In: *Comput. Methods Appl. Mech. Eng.* 191.39-40 (2002), pp. 4341–4370.

[80] James K. Guest and Jean H. Prévost. "Optimizing multifunctional materials: Design of microstructures for maximized stiffness and fluid permeability". In: *Int. J. Solids Struct.* 43 (2006), pp. 7028–7047.

[81] James K. Guest and Jean H. Prévost. "Design of maximum permeability material structures". In: *Comput. Methods Appl. Mech. Eng.* 196.4-6 (2007), pp. 1006–1017.

[82] TJ Lu, Howard A Stone, and MF Ashby. "Heat transfer in open-cell metal foams". In: *Acta Mater.* 46.10 (1998), pp. 3619–3635.

[83] Anton Du Plessis et al. "Properties and applications of additively manufactured metallic cellular materials: A review". In: *Prog. Mater. Sci.* 125 (2022), p. 100918.

[84] Daniel Leitner et al. "A dynamic root system growth model based on L-Systems: Tropisms and coupling to nutrient uptake from soil". In: *Plant Soil* 332.1 (2010), pp. 177–192.

[85] The MathWorks, Inc. *MATLAB, Version 9.13.0 (R2022b).* 2022.

[86] Przemyslaw Prusinkiewicz and Aristid Lindenmayer. *The algorithmic beauty of plants.* Vol. 263. New York, NY: Springer Science & Business Media, 1990.

[87] Betty Klepper and Thomas C Kaspar. "Rhizotrons: Their development and use in agricultural research". In: *Agron. J* 86.5 (1994), pp. 745–753.

MOX Technical Reports, last issues

Dipartimento di Matematica
Politecnico di Milano, Via Bonardi 9 - 20133 Milano (Italy)

65/2025 Pottier, A.; Gelardi, F.; Larcher, A.; Capitanio, U.; Rainone, P.; Moresco, R.M.; Tenace, N.; Colecchia, M.; Grassi, S.; Ponzoni, M.; Chiti, A.; Cavinato, L.
MOSAIK: A computational framework for theranostic digital twin in renal cell carcinoma

64/2025 Celora, S.; Tonini, A.; Regazzoni, F.; Dede', L. Parati, G.; Quarteroni, A.
Cardiocirculatory Computational Models for the Study of Hypertension

63/2025 Panzeri, S.; Clemente, A.; Arnone, E.; Mateu, J.; Sangalli, L.M.
Spatio-Temporal Intensity Estimation for Inhomogeneous Poisson Point Processes on Linear Networks: A Roughness Penalty Method

62/2025 Rigamonti, V.; Torri, V.; Morris, S. K.; Ieva, F.; Giaquinto, C.; Donà, D.; Di Chiara, C.; Cantarutti, A.; CARICE study group
Real-World Effectiveness of Influenza Vaccination in Preventing Influenza and Influenza-Like Illness in Children

61/2025 Coclite, A; Montanelli Eccher, R.; Possenti, L.; Vitullo, P.; Zunino, P.
Mathematical modeling and sensitivity analysis of hypoxia-activated drugs

60/2025 Antonietti, P. F.; Caldana, M.; Gentile, L.; Verani M.
Deep Learning Accelerated Algebraic Multigrid Methods for Polytopal Discretizations of Second-Order Differential Problems

59/2025 Wolf, F.; Botteghi, N.; Fasel, U.; Manzoni, A.
Interpretable and efficient data-driven discovery and control of distributed systems

58/2025 Pivato, C.A.; Cozzi, O.; Fontana, N.; Ieva, F., et al.
Clinical outcomes of percutaneous coronary interventions after transcatheter aortic valve replacement

57/2025 Guagliardi, O.; Masci, C,; Breschi, V; Paganoni A, ; Tanelli, M.
A Novel DNA-Inspired Framework to Study University Dropout: Insights from Politecnico di Milano

56/2025 Tonini, A.; Bui-Thanh, T.; Regazzoni, F.; Dede', L; Quarteroni, A.
Improvements on uncertainty quantification with variational autoencoders